ABSTRACT

BARRETTE, ANDREW GIBSON. Ultrafast Optical Studies of Amplified Spontaneous Emission in Hybrid Organic-Inorganic Perovskites. (Under the direction of Kenan Gundogdu).

Lead-halide perovskites of the form CLH_3 have exhibited promising chemical tunability and ease of synthesis via solution processing techniques, which have led to surprisingly low defect densities and outstanding carrier properties. One of the leading materials in this category is methylammonium lead iodide ($MAPbI_3$), which has been found to have paradoxically high carrier mobilities and lifetimes, in addition to highly efficient exciton dissociation into free carriers due in part to the MA cation, which is able to rotate to screen carriers. Having remarkably low excitation density thresholds for amplified spontaneous emission (ASE), lead-halide perovskites have also found use as lasing media, with chemical substitutions allowing for easy tunability of ASE energy, and with much work being devoted to the study of various microstructures with inherent resonances that enhance ASE output. One such microstructure is inherent and forms when the material temperature is lowered below the phase transition temperature at 150K. The phase transition from tetragonal phase (TP) to the orthorhombic phase (OP) is incomplete, with some small TP inclusions remaining. As TP has a lower bandgap, these inclusions draw in carriers excited in OP (the primary phase by volume below 150K), where they become highly concentrated, thus resulting in very low effective ASE threshold and allowing for sustainable continuous lasing. Such low threshold ASE is necessary for high efficiency lasing applications, such as nanoscale on-chip lasers, but little is known about the species and timescale of ASE in this system. In this work, we use ultrafast transient absorption and time-domain terahertz spectroscopy to study carrier dynamics in $MAPbI_3$ in the low temperature (TP inclusion) regime, and uncovered the timescale and underlying carrier mechanisms of ASE. We find that ASE appears at an excitation density where transfer of excitons from OP to TP halts due to filling of TP inclusions. At this carrier density, ASE occurs and is quenched by exciton dissociation after 5ps. Thus ASE occurs within 5ps in this system, suggesting applications such as ultrafast optical switches and amplifiers for ultrashort pulse tuning. These applications will require optimization of carrier transport and ASE lifetime for maximum bandwidth, which our findings indicate will require control of TP inclusions size and exciton screening.

Ultrafast Optical Studies of Amplified Spontaneous Emission in Hybrid Organic-Inorganic Perovskites

by
Andrew Gibson Barrette

A dissertation submitted to the Graduate Faculty of
North Carolina State University
in partial fulfillment of the
requirements for the Degree of
Doctor of Philosophy

Physics

Raleigh, North Carolina

2018

APPROVED BY:

Daniel Dougherty	Franky So
Alex Kemper	Kenan Gundogdu Chair of Advisory Committee

DEDICATION

To my parents, Tom and Diana Barrette, whose never-ending love and support allowed me to strive for greatness.

ACKNOWLEDGEMENTS

I would like to acknowledge Felix Castellano and Evgeny Danilov for use of and training on the transient absorption spectroscopy equipment, and Nuh Gedik and Daniel Pilon for guidance during initial alignment of THz spectroscopy experiment. I would like to acknowledge Harold Ade, who served on my committee until recently, and has been a mentor throughout my PhD.

TABLE OF CONTENTS

LIST OF FIGURES

Chapter 1

Introduction

Methylammonium lead iodide ($MAPbI_3$) has made waves recently as a cheap solution-processable crystal with remarkable power conversion efficiency of 11% in 2012 and now exceeding 22% [1]. $MAPbI_3$ is also now known to be an efficient light emitter, due in part to its high mobility and long carrier diffusion lengths which make it a good solar cell [2]. The $MAPbI_3$ crystal structure is essentially a lead-iodide lattice with an interstitial methylammonium cation in each lead-iodide cage. It has three known structural phases: Cubic phase existing above 310K, orthorhombic phase (OP) existing below 150K, and tetragonal phase (TP) in-between. The unit cell of TP is slightly twisted relative to that of cubic phase, and the organic cation can freely rotate in TP. In OP, the unit cell has an additional twist and the cation is frozen in a particular orientation. This has profound effects on the electronic properties of the system as the rotation of the cation screens carriers, thus lowering the dielectric constant in TP.

This material is also interesting because it exhibits a phenomenon known as amplified spontaneous emission (ASE) [3–8]. ASE is the spontaneous amplification of photoluminescence (PL) in a material (described in greater detail in Ch.2). Like lasing, ASE is quenched by re-absorption of emission and is thus more efficient when the system is heavily bleached (excited). Also, both processes require efficient light emission, implying low nonradiative recombination. In fact, such amplification processes can only occur when a photon passing through the material has a higher probability of stimulating emission than being absorbed. The biggest differences between these too effects are that laser output is far more spatially coherent, due to the implementation of feedback via a cavity, and temporally coherent due to the use of a coherent seed. However, because the underlying mechanisms are very similar, strong ASE is usually a good indicator of potential laser applications. This is perhaps best emphasized in the recent work of N. C. Giebink's group [9], which bridged the gap from ASE to lasing in $MAPbI_3$ by producing continuous-wave (CW) lasing for the first time. The catch: CW lasing can be achieved below the TP-to-OP structural phase transition at 150K, but only from TP inclusions in the OP bulk

(Fig.1.1).

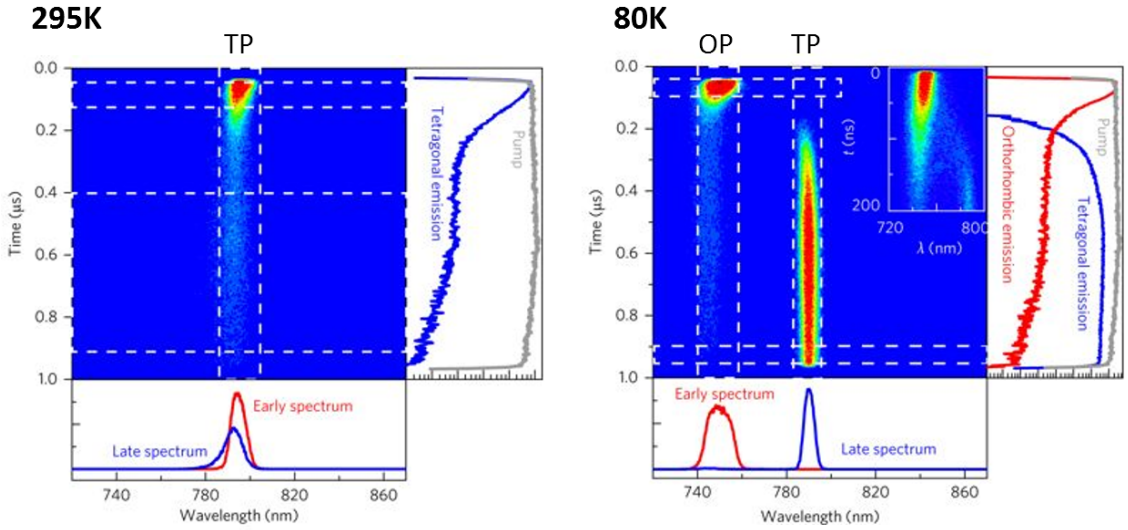

Figure 1.1 Continuous-wave pumping of $MAPbI_3$ in DFB geometry at room temperature (left) results in lasing that quickly dies. At 80K (right), lasing from tetragonal inclusions is sustainable. [9]

It has already been observed that TP is the primary PL emitter below 150K, even though absorption suggests that OP is the primary absorber [10, 11]. The apparent existence of TP even at OP temperatures (sub-150K) has been explained in terms of TP inclusions that remain, despite the bulk phase transition, due to the build-up of strain at domain interfaces (Fig.1.2). Accordingly, ASE and the aforementioned CW lasing are also observed from TP, even below 150K when the bulk is primarily OP. The important discovery by Giebink was that CW lasing (effectively, ASE sustained by CW pump) can be achieved in TP below the phase transition temperature but not above it (when the entire system is TP), and this was explained in terms of a picture that has been developing in the $MAPbI_3$ community in which TP inclusions (bandgap 1.55eV) in the OP bulk (bandgap 1.65eV) act as low-energy wells in which carriers collect in high concentrations, resulting in more efficient PL and hence ASE, as depicted in Fig.1.2. Thus, the finding that CW lasing can only be sustained from TP inclusions in the OP bulk is consistent with previous findings.

While much progress has been made in understanding the nature of TP inclusions and their macroscopic role as nanocrystalline ASE centers, the community is still lacking a cohesive microscopic picture of the carriers responsible for ASE. It is currently believed that, below 140K, TP inclusions make up a small fraction of the total volume according to absorption contribution, and thus carriers excited in OP should reach high densities after transferring

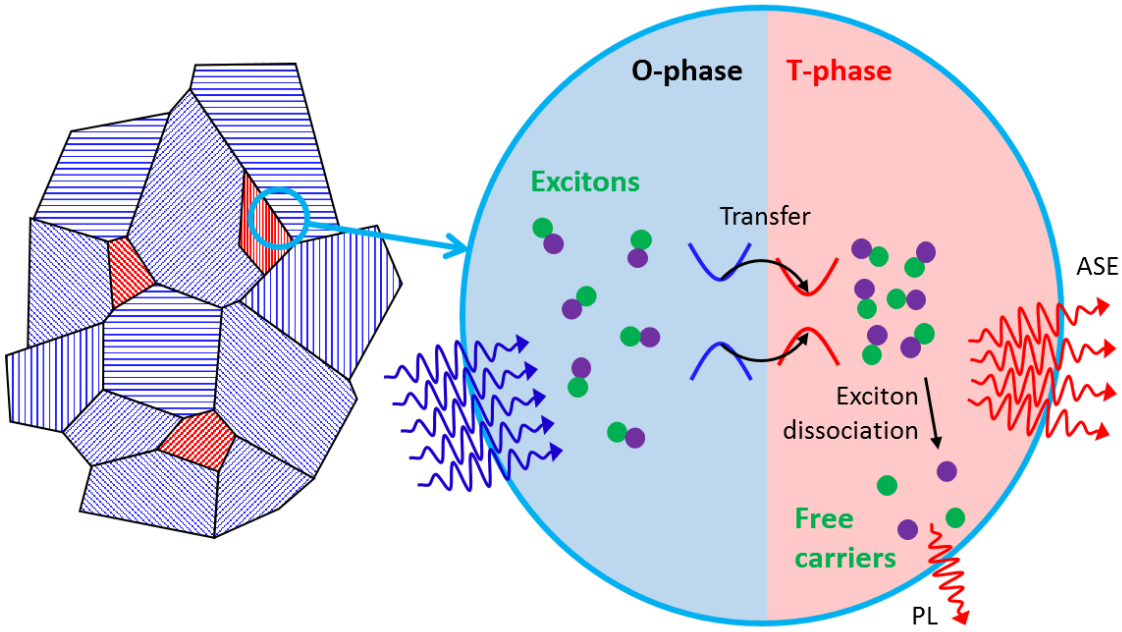

Figure 1.2 (from left) Below 150K, TP inclusions (red) remain within the OP bulk. When OP is excited, excitons are generated, which quickly transfer to the lower-energy TP sinks. There, they dissociate into free carriers and emit PL on the timescale of nanoseconds. Somewhere in this process, ASE is emitted.

to the TP inclusions. This concentration effect should have a strong temperature dependence since the existence of TP inclusions is discontinuous about the phase transition temperature. Furthermore, while it is currently believed that TP carriers are mostly free while OP carriers are bound excitons, the nature of carriers in $MAPbI_3$ has been the subject of much debate in $MAPbI_3$ literature. A recent study [12] suggested that charged carriers become dressed by phonons, resulting in quasiparticles (large polarons) which couple carriers across long distances and ultimately facilitate ASE. The more recent studies of ASE have led to such speculations about the carrier species responsible for ASE, but still no conclusive evidence has been found for or against these possibilities.

As the dynamics of carriers before and during ASE having never been explicitly measured, it is no wonder that the microscopic mechanisms related to ASE are not yet understood. Therefore, to address these problems, we have explored the experimental search space in a critical region that has not previously been studied: Low temperature (OP with TP inclusions), high fluence (above ASE threshold), and small timescales (relevant to fundamental mechanisms). Furthermore, we use a comprehensive set of tools, including terahertz spectroscopy (giving conductivity-resolved population dynamics), and transient absorption spectroscopy (giving energy-resolved

population dynamics), in addition to steady state absorption and emission, altogether allowing us to paint a much needed picture of carriers just after excitation.

The remainder of this dissertation is separated into three chapters. In Chapter 2, we provide theoretical background on ASE as well as background information on $MAPbI_3$, further discussing the interplay between TP and OP, the various charge species which are thought to exist, and also basic concepts relevant to understanding ASE. In Chapter 3, we describe the experiments used to study $MAPbI_3$, including steady-state measurements such as absorption and photoluminescence and time-resolved measurements such as transient absorption spectroscopy, and terahertz spectroscopy. Finally, in Chapter 4 we disclose our experimental results from each measurement, including a discussion section consisting of deductions and interpretations of the data.

Chapter 2

Background

2.1 Amplified spontaneous emission

ASE occurs when spontaneously-emitted light within a material is more likely to stimulate emission (SE) than absorb, a criteria known as optical gain. Experimentally, ASE takes the form of a narrow emission band slightly below the bandgap and PL peak (Fig.2.1a). As PL occurs at the absorption band edge, the high energy side of the PL spectrum is easily reabsorbed by the material and thus ASE occurs at the low energy side of the PL spectrum where the product of transmission and emission, and thus also the gain, has a maximum.

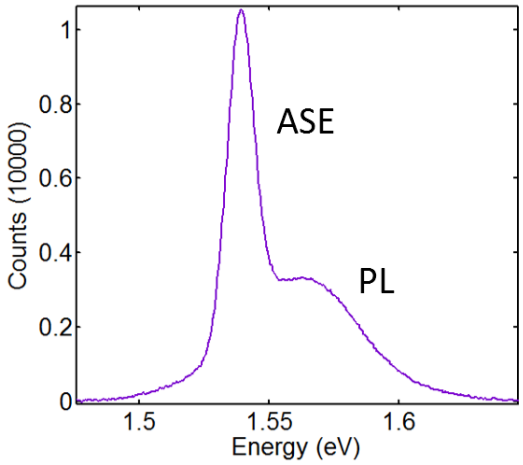

Figure 2.1 Emission spectrum of $MAPbI_3$ at 80K, showing PL at 1.56eV and narrow ASE peak at slightly lower energy.

For a theoretical treatment of ASE, we can start with a basic semiconductor band picture where carriers exist on parabolic bands separated by bandgap E_g (Fig.2.2a). Photons with sufficient energy can excite electrons from valence band ($E = E_v - \hbar^2 k^2/2m_v$) to conduction band ($E = E_c + \hbar^2 k^2/2m_c$), thus leaving behind holes in the valence band. Electrons and holes initially cool to the band edges (at E_c and E_v, respectively) forming quasi-Fermi distributions, so called because we are considering a timescale long enough for carriers to come to equilibrium at the band edges (usually <1ps) yet short enough that electrons have not had time to relax completely to their true ground state in the valence band. This implies that spontaneous emission is relatively slow and can be ignored as a population decay mechanism on this timescale. The percentage of states filled at a given energy follows a Fermi function [13]. For conduction and valence bands, these have the respective forms

$$f_c(E_1) = \frac{1}{1 + exp[(E_1 + E_{ph} - F_c)/k_B T]}, \quad and \tag{2.1}$$

$$f_v(E_1) = \frac{1}{1 + exp[(F_v - E_1)/k_B T]}, \tag{2.2}$$

where E_1 is the energy of a hole in valence band, $F_{c/v}$ is the Fermi energy for electrons in conduction band and holes in valence band, $k_B T$ is the ambient thermal energy, and $E_{ph} > E_g$ is a specified photon energy which may trigger SE or absorption (notice that we have defined electrons in the conduction band with respect to the hole at energy E_{ph} below).

The joint density of states (DOS), ρ_{jnt}, gives the DOS that can contribute to an absorption or SE reaction with the given photon energy. Given that absorption and SE occur between an electron and hole at the same k-point due to optical selection rules, E_1 (and likewise, E_{ph}) defines a sphere of contribution in 3D k-space. ρ_{jnt} is the state density at the surface of this sphere with respect to energy $\rho_{jnt} \sim k^2(dk/dE) \sim (E_v - E_1)^{1/2}$, as depicted in Fig.2.2b. The rates of SE and absorption then have the form

$$R_{SE} = B\rho_{ph}\rho_{jnt} f_v(E_1) f_c(E_1), \tag{2.3}$$

$$R_{abs} = B\rho_{ph}\rho_{jnt}(1 - f_v(E_1))(1 - f_c(E_1)), \tag{2.4}$$

where B is the corresponding Einstein coefficient related to transition probability and ρ_{ph} is the population density of photons at E_{ph}. For SE we require a hole in the valence band and an electron in the conduction band, whereas for absorption we require the negation of these conditions. The criteria for optical gain is that $R_{SE} > R_{abs}$ and, as everything cancels out except the Fermi functions, it is easy to show that this implies that

$$E_{ph} < F_c - F_v. \tag{2.5}$$

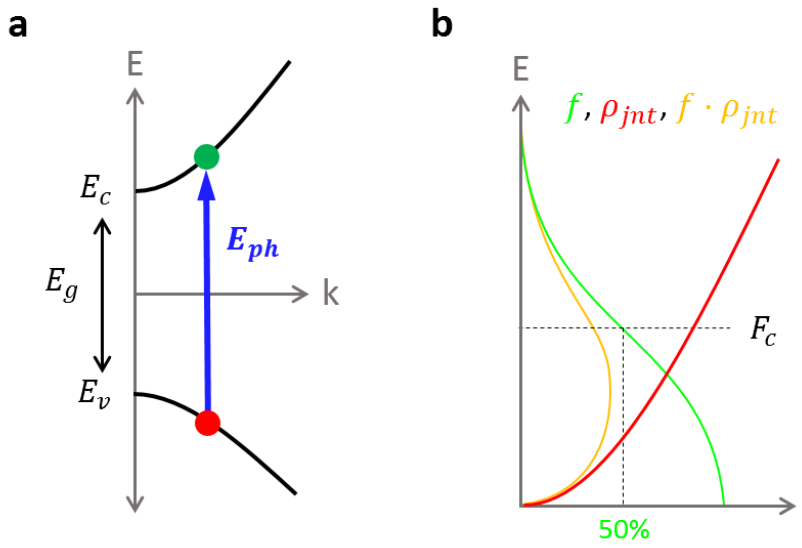

Figure 2.2 (a) Electrons and holes, in parabolic valence and conduction bands with extrema at E_v and E_c and bandgap of $E_c - E_v = E_g$, are coupled by a photon with energy E_{ph}. (b) On timescales much shorter than spontaneous recombination lifetime, carriers settle to bottom of band, forming a "quasi-Fermi" distribution, which when multiplied by the density-of-states for a parabolic band gives the carrier density per energy.

As carriers are added to the system, the Fermi energies are pushed outward. Once the density is high enough that $F_c - F_v$ encompasses the bandgap, optical gain can occur at energies near the band edge. That is to say, the population is "inverted" at these energies. In practice, the density threshold for optical gain for a particular E_{ph} is calculated numerically: Carrier density for a particular Fermi energy is found by integrating over the product of density of states and Fermi function, and by trial and error one can find the lowest carrier density such that eqn.2.5 is satisfied.

While we assumed spontaneous emission to be negligible as a decay mechanism, when it does occur it can be amplified to produce ASE. SE and absorption processes are actually the same and differ only by the phase of the photon emitted: For absorption it's phase is 180^o from the input photon, whereas for SE it is in-phase. Energy and polarization of the stimulated photon are also generally considered to be identical to that of the input photon. The formal reason for this comes from quantum mechanics, where processes involving the addition of a photon invoke the photon raising operator, resulting in a prefactor of $\sqrt{N_{ph}+1}$, where N_{ph} is the current number of photons, which is then squared in Fermi's Golden Rule (this is why $R_{SE} \sim \rho_{ph}$). Therefore other energies, polarizations, and phases of the stimulated photon aren't impossible, they are just less likely than the dominant mode. This implies that inserting a seed

to an inverted population will result in a coherent output that is much more spatially and temporally coherent than if the inversion process is allowed to begin spontaneously, as is the case for ASE. This and the lack of feedback result in ASE being not particularly polarized or directional compared to laser light.

Other factors can inhibit optical gain, including non-radiative mechanisms such as trap-assisted recombination and Auger recombination, which compete at high carrier densities [14]. Radiative decay channels can also compete with ASE by shortening carrier lifetimes, though this is sometimes desirable to allow for lasers with high-frequency modulation. Studying these relationships between recombination pathways and ASE is of particular importance in $MAPbI_3$, where carrier mobilities and recombination rates are still considered to be somewhat anomalous. ASE is also impacted by microscopic material structure, which can facilitate charge separation or, conversely, concentration, among other phenomena. Thus studying ASE in various types of nanostructures has been a theme in some previous $MAPbI_3$ research [6–8, 15].

Finally, the more accurate many-body theory of ASE makes more accurate predictions by doing away with the assumption that carriers are localized in k-space and considering microscopic correlations that potentially make the ASE process more nuanced. In any case, the observation of ASE in a material is an indication that the material might make a suitable lasing medium, hence optimization of the processes and structures that impact ASE is critical for further laser development.

2.2 Hybrid organic-inorganic perovskites

Chemists draw a conceptual line between organics and inorganics. On one hand, organics contain carbon as a base component. Carbon's four valence electrons make it structurally versatile, allowing many complex molecular structures with tunable electronic properties. This makes organics ideal for the design of functionalized molecules with application-specific energy structures. This and other advantages like low cost and light weight have been strong motivators for the development of organic replacements for traditional Si-based solar cells, with one of the main limitations being the hopping-limited (low) mobility of localized carriers in organic systems such as small molecules and polymers. On the other hand, inorganics consist of elements that bond strongly and thus form highly regular crystal structures. These crystal structures are further divided into conductors, semiconductors, and insulators with resonances depending on composition and processing. When crystallinity can be controlled, the regularity of inorganic structures admits long-range conduction of charges and other exotic coherent effects.

Recently, attention has been drawn to the study of hybrid organic-inorganic perovskites (HOIP) consisting of an inorganic lattice with interstitial organic cation, often thought of as an inorganic grid of face-centered cages with each cage containing an organic cation. This

combination of easy functionalization from organics with the long-range transport ability from inorganics has culminated in the discovery of many interesting materials where the interplay between organic molecule and inorganic lattice is sometimes unexpectedly favorable. Additionally, HOIPs can be synthesized by simple solution processing techniques that are so easy to perform that they're often jokingly referred to as "kitchen chemistry".

One HOIP of recent interest to the community is $CH_3NH_3PbI_3$, methylammonium lead iodide ($MAPbI_3$), which was discovered to be a remarkable solar cell medium in the 2000s. Since then, the record power conversion efficiency (PCE) of $MAPbI_3$ solar cells exceeded 20% in 2015 [16, 17], and this success has been attributed to a combination of exceptional material properties including low bandgap, 100% charge separation efficiency (due to thermal and coulombic screening), high mobility (due to the highly polarized PbI_3 lattice), and recombination times vastly exceeding the theoretical limit [2, 18].

2.3 Methylammonium lead iodide

$MAPbI_3$ has three structural phases: Cubic phase above 310K, tetragonal phase (TP) from 310K down to 150K, and orthorhombic phase (OP) below 150K. The cubic structure is a face-centered lead-iodide lattice with interstitial methylammonium cations, where the lattice unit is often pictured as a cage containing a dipolar cation. With the main motivation for its study being that solar cells in practical applications (i.e. absorbing sunlight all day) will likely get hot enough to transition to this phase, it is perhaps ironic that the cubic phase is the lesser studied of the three. TP and OP are similar to the cubic phase but with subsequent twistings of octahedral lead-iodide units (Fig.2.3a). The TP and OP phases have been studied to a greater extent due to the effect of the cation (Fig.2.3b), which in TP can freely rotate but is fixed in OP. Screening resulting from this rotational degree of freedom has a profound effect on dielectric constant and hence on exciton dissociation, transport, and diffusion lengths [19, 20] (more on this later).

A phenomenon which was not resolved until recently is the predominance of PL at the TP energy below the phase transition, where steady-state absorption studies confirm that the primary absorber is OP. It is now believed that this results from the energetic stability of small TP inclusions which never transition, apparently even down to 5K [10]. These inclusions are thought to balance strain resulting from the structural phase transition. The lack of apparent TP absorption below the phase transition suggests that the inclusions have a small volume fraction yet are highly efficient emitters relative to OP. Their low bandgap relative to OP suggests that they act as wells in which carriers collect. To what extent the crystal strain encourages carrier/exciton drift to these wells is still unknown, but it has also been suggested that emission of heat by carriers during cooling may result in the active formation of such TP inclusions [9].

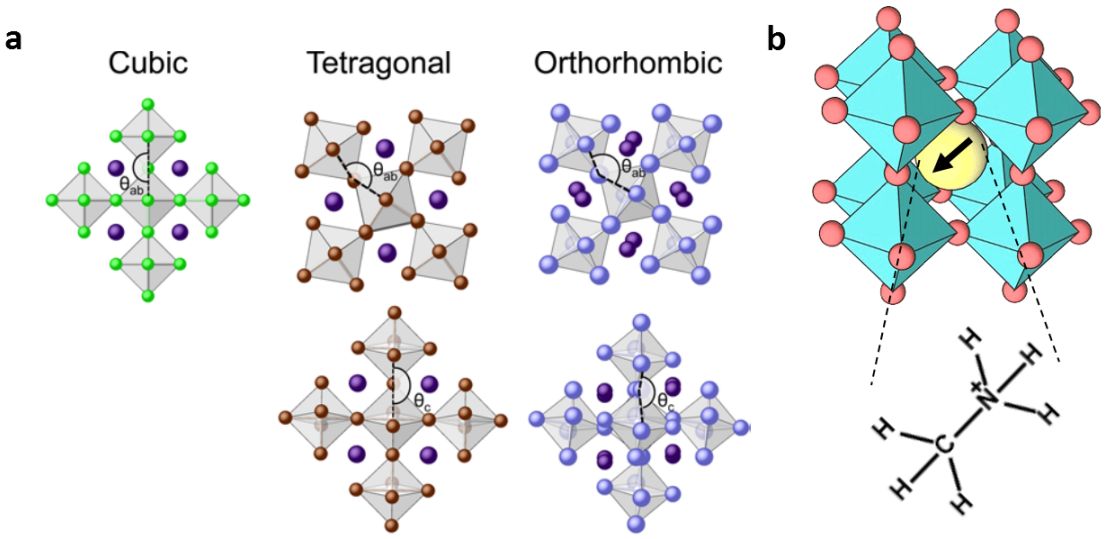

Figure 2.3 (a) $MAPbI_3$ has three crystal phases: Cubic (T>310K), tetragonal (150K<T<310K) and orthorhombic (T<150K) [21]. (b) In $MAPbI_3$, the cation is a methylammonium dipole which can discretely rotate between one of six faces in tetragonal phase, but in orthorhombic phase is frozen in a particular orientation.

In $MAPbI_3$, ASE typically occurs in TP phase, even below the phase transition temperature. If carriers collect in TP inclusions, then it follows that smaller inclusions (presumably existing at lower temperatures) will result in more efficient ASE due to higher densities of carriers concentrated in a smaller volume.

2.4 Free carriers versus excitons in $MAPbI_3$

Cation screening in TP lowers the dielectric constant by a factor of 10, decreasing exciton binding energy and allowing excitons to dissociate into free carriers in TP where the exciton binding energy is thought to be ∼10meV [12, 19]. It is typically assumed that an absorbed photon results in an exciton in the material, except in systems where the exciton binding energy is near or less than the available thermal energy k_BT, which is 25meV at room temperature. The creation of excitons upon optical excitation is often pointed out based on the existence of a resonance at the absorption band edge attributed to strong coupling between the exciton dipole and light field. This "excitonic feature" is usually absent in $MAPbI_3$ at room temperature, suggesting that free carriers are excited initially, whereas it is usually visible in the related lead-bromide perovskite, which have larger exciton binding energy [22] (Fig.2.4a). Furthermore, an excitonic feature is usually observed in $MAPbI_3$ near and below 150K [23] (Fig.2.4b) and this

is explained in terms of OP having a rotationally-frozen cation and thus stronger excitonic coupling.

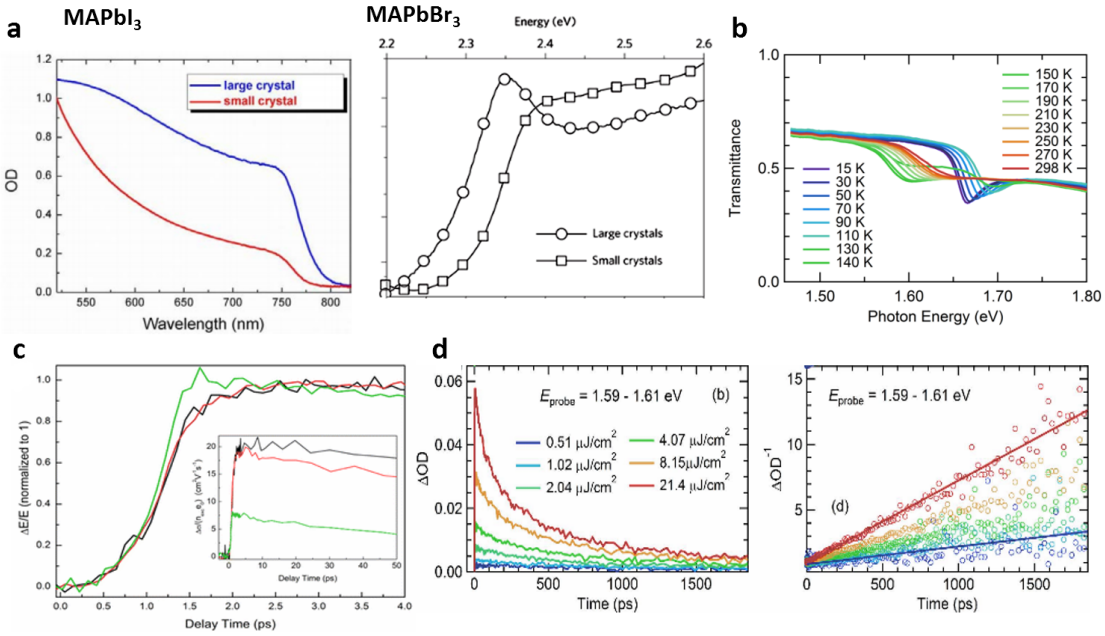

Figure 2.4 (a) Room temperature absorption spectrum of $MAPbI_3$ as well as $MAPbBr_3$ which has higher binding energy, showing distinct excitonic resonance in the latter but none in the former. [22]. (b) $MAPbI_3$ transmission spectrum as a function of temperature [23]. A sharp transition between TP and OP occurs at 150K. (c) Fast 1ps rise of THz conductivity signal in $MAPbI_3$, suggesting that free carriers form immediately [24]. (d) Photobleaching dynamics (left) show carrier population decay. Inverses of dynamics curves (right) are linear, indicating bimolecular recombination indicative of free carriers. [23]

Other evidence that free carriers are indeed the predominant species in TP include population dynamics measurements. Such measurements (described in detail in the next section) can produce curves tracking free or total carrier populations on picosecond timescales. Free carriers can be tracked via photoconductivity, which is sensitive to the motion of charges (free carriers being charged). Studies using this measurement found that free carrier population rises within 1ps after excitation [24] (Fig.2.4c), effectively instrument-response limited, suggesting that the initially excited species is either free carriers or excitons that immediately dissociate into free carriers. The total charge population can be tracked via transient absorption dynamics, which correspond to total carrier populations (free or bound). Whether carriers are free or bound can then be deduced based on kinetic modeling: Bound carrier recombination is a 1st-order process

$(dn/dt \sim -n)$ whereas free carrier recombination is a 2nd-order process $(dn/dt \sim -n^2)$. Studies using this measurement found that TP dynamics follow the 2nd-order rate equation indicative of free carrier recombination [23] (Fig.2.4d).

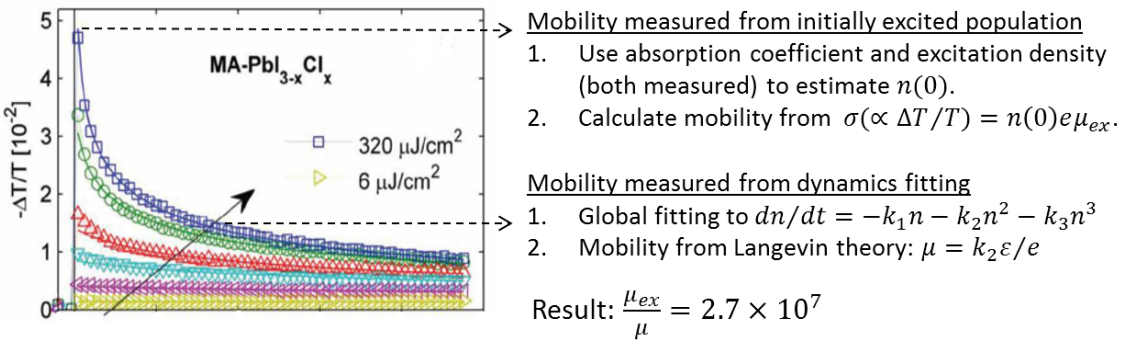

Figure 2.5 Outline of Herz's analysis. The initially excited population density can be calculated, and thus the initial mobility can be calculated from the initial photoconductivity, $\Delta\sigma \propto -\Delta T/T$, given that $\Delta\sigma = ne\mu$. Assuming the mobility is static, the previous calculation can then be compared to the mobility as calculated from the shape of the dynamics curves. The curves ca be fitted to extract the 2nd-order decay constant k_2, which is related to mobility through Langevin's theory of bimolecular recombination.

Initial studies of $MAPbI_3$ found long carrier diffusion lengths ($\sim 1\mu$m) compared to typical solution-processed semiconductors ($\sim$10nm) [2, 25, 26]. Diffusion lengths depend on recombination rate (determining lifetime) and mobility (determining how far a carrier can travel in a given time). However, in systems dominated by bimolecular recombination where carrier motion is ballistic in nature, there is a relationship between recombination rate and mobility. In principle, bimolecular recombination is mediated by how easily carriers can "capture" each other, so carriers that are highly mobile will be able to traverse space faster and find a partner for recombination more easily. Langevin theory dictates that materials with high mobility, μ, should have high bimolecular recombination rate, k_2, following the relation $k_2/\mu = e/\varepsilon$ and thus short carrier lifetimes. However Wehrenfennig et al. [2, 27] measured k_2 by modeling THz conductivity decay curves according to the generic rate equation $dn/dt = -k_1 n - k_2 n^2 - k_3 n^3$, finding $k_2 = 9 \times 10^{-10}\text{cm}^3\text{s}^{-1}$, and by Langevin's equation found that $MAPbI_3$ should have $\mu = 6.2 \times 10^{-5}\text{cm}^2\text{V}^{-1}\text{s}^{-1}$. And yet when extracting the mobility from the initial conductivity via the definition of conductivity, $\Delta\sigma = e\mu n_{exc}$ where n_{exc} is the initially excited population density, they found that $\mu = 8\text{cm}^2\text{V}^{-1}\text{s}^{-1}$, five orders of magnitude above the theoretical limit based on carrier recombination rates (Fig.2.5). This suggests a breakdown of the generic

Langevin theory in which carrier mobility and bimolecular recombination rate have a particular relationship. The suppression of bimolecular recombination has been met with several explanations, but has still not been resolved. Wehrenfennig et al. initially suggested that electrons and holes travel along separate pathways in the crystal, but this suggestion never gained much traction. I'll mention a few other explanations in the next section.

2.5 Recent developments

Recent research developments have resulted in several other explanations for the inexplicably long carrier lifetimes. One explanation is that spin-momentum coupling ($\sigma \cdot p$ in the Hamiltonian) results in a spin-energy splitting with sign depending on momentum. In the band picture, this corresponds to a splitting of the conduction band along the k-axis, also known as Rashba splitting (Fig.2.6a). When a charge is excited to a Rashba-split conduction band, it will relax to an indirect minimum at $\Delta k > 0$ or $\Delta k < 0$, depending on the spin of the excited electron. This indirect position in k-space results in radiative recombination being quenched, and hence long carrier lifetimes [28–30].

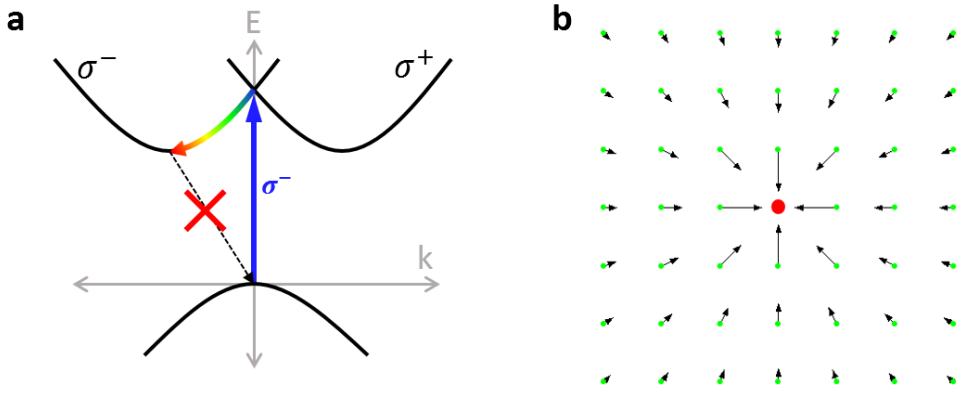

Figure 2.6 (a) Rashba splitting: When a conduction band electron moving in a particular direction experiences a force proportional its spin (e.g. under an applied magnetic field) the conduction band splits with respect to momentum. A carrier excited vertically from the valence band will then relax to an indirect position in the conduction band, reducing its ability to recombine. (b) Polaronic distortions of the lattice, which screen a carrier from scattering sources outside of the "shell".

Another proposed explanantion for the apparent isolation of electrons and holes is polaronic screening (Fig.2.6b) whereby lattice distortions (meaning either Pb-I deformations or cation rotations) result in fields that cancel out carrier-carrier and carrier-impurity interactions [12, 31, 32].The possibility of the formation of polarons in $MAPbI_3$ has recently expanded into its

own field, sparked by the observation of a so-called hot-phonon bottleneck whereby excited carriers are seemingly isolated from normal cooling pathways and remain at high energy in the band. In $MAPbI_3$, polaron screening has been used to explain the observation of hot carriers lasting for hundreds of picoseconds, and is also a convenient explanation for the aforementioned paradoxical combination of high mobility and low bimolecular recombination rate [12, 33–35]. The bottleneck has been rationalized via several different mechanisms, mainly Auger heating whereby high carrier densities allow for three-body interactions where recombination energy is released in the form of a hot carrier, isolation between carriers and optical phonons due to polaron formation or a reduced phonon density of states, and inability of optical phonons to decay into acoustic phonons, which may then propagate to the far field in the crystal [33,36–39]. Nevertheless there is still much disagreement in the literature on what causes this effect in $MAPbI_3$ and related perovskites.

Direct proof of the existence of polarons in $MAPbI_3$ does not yet exist, but the existing evidence suggests that they may occur in TP where dielectric constant is already known to be relatively low. More exotic hypotheses suggest that the polaronic screening may be associated with the rotational degree of freedom of the cation [12,19,34]. This rotational degree of freedom was found to have a response time of $\sim$2ps [31], which may explain why excitons are unstable in TP on picosecond timescales.

This last suggestion is intriguing as it may allow for simultaneous carrier isolation (leading to high mobility) and long-range polaronic correlations facilitating efficient recombination necessary for ASE. The problem at hand is that all of these explanations for the paradoxically-low carrier recombination - whether it is due to separate pathways for electrons and holes, Rashba splitting, or polaronic screening - must answer for the existence of strong ASE which suggests that carriers in TP are somehow able to interact with each other despite apparently being isolated from other Coulombic scattering mechanisms. If the time-scale of ASE has not yet been explicitly studied then could the assumption that it is emitted from free carriers be inappropriate? What will ASE dynamics reveal about the carrier species that is excited initially, and about how it evolves on picosecond timescales? Can we support one of the hypotheses previously posited in the literature or will ultrafast measurements suggest a new timeline altogether?

Chapter 3

Experimental methods

3.1 Steady state measurements

A good starting point for any ultrafast spectroscopy study is measurement of steady state optical response because the discovered features can often later be identified in transient spectral measurements. The two such techniques used in this work are absorption and PL.

Absorption measurement involves simply the measurement of transmitted white light (Fig.3.1a), and is expressed as optical density (OD, absorbance), where the proportion of absorbed light at a given frequency ω is given by $A(\omega) = 1 - 10^{-OD(\omega)}$. This expression can be related to Beer's law for a sample of thickness l: $A(\omega) = 1 - e^{-\alpha(\omega)l}$, where α is known as the attenuation coefficient. This form is useful because it represents the population of excited carriers as an exponential distribution decaying into the sample at a rate of α, so $1/\alpha$ is sometimes used as an approximation of the depth of the carrier population when, for example, one needs to find carrier volume in order to calculate carrier density. Absorption spectra generally consist of low absorption at energies below the bandgap with a sudden rise in absorption at the band edge, which may be accompanied by a peak associated with the increased coupling of light with excitons, and rising "continuum" absorption at energies above the bandgap (Fig.3.1b,c).

PL measurement involves exciting a sample and observing the light subsequently emitted. In PL experiments, typically the sample is excited above the bandgap and emission is Gaussian distributed about the band edge where coupling between the conduction and valence band carriers is relatively high. In-between these two steps, carriers radiate longitudinal optical phonons (Frohlich interaction [40]) in order to minimize energy and relax to toward the band edges. When this process has completed, carriers at the band edge are in quasi-equilibrium and can (if they haven't already) thermalize to form a Fermi-Dirac distribution, which manifests as an exponential tail on the high-energy side of the PL spectrum. This tail, with respect to energy E, is sometimes fitted with the equation $e^{-E/k_B T_e}$ to extract the temperature of excited carri-

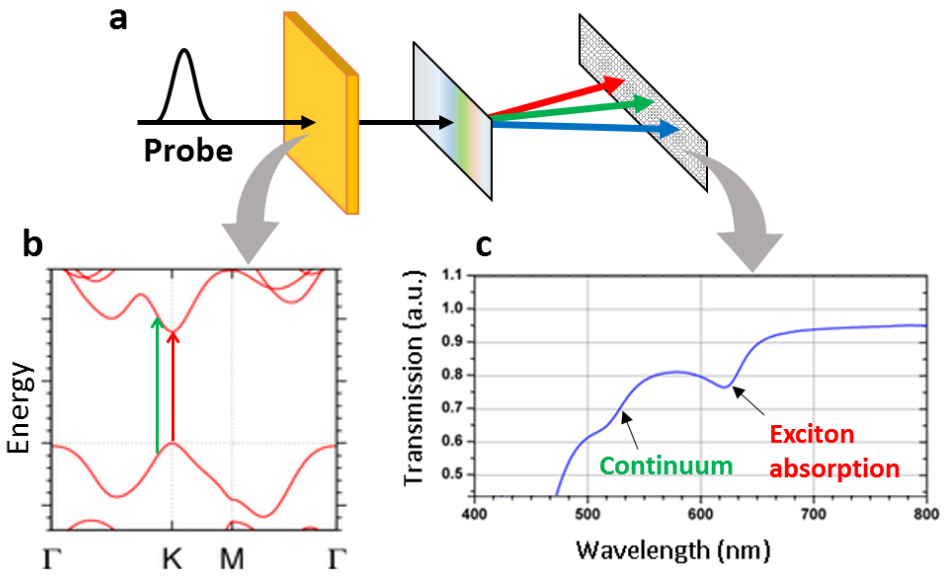

Figure 3.1 (a) Light absorption is measured by passing a "probe" beam through a sample and measuring transmission. The frequency of the probe is resolved using a grating and CCD. A broadband probe consists of many superimposed modes. This is like multiplexing many different transmission experiments so that they can be performed in a single shot. Furthermore, the phases of the modes within the probe can be set so that the probe is pulsed in time/space. This temporal localization is necessary for time-resolved experiments. (b) In the energy-space picture, a photon is absorbed and is excited from the valence band to the conduction band. (c) This absorption results in a decrease in probe transmission above the bandgap energy. At the band edge, conduction band electrons and valence band holes can bind together to form excitons.

ers, T_e. This technique is useful for tracking carrier cooling within the conduction and valence bands. PL is emitted when an electron and hole recombine but the converse is not true: The absence of PL at the band edge does not preclude the existence of carriers but instead could also indicate that carrier recombination is nonradiative, in which case recombination energy is either given to other carriers (Auger) or released as phonons.

3.2 Pump-probe

Transient measurements are used to track the properties of a sample over time and generally take the pump-probe form where the sample is pumped and then probed after some delay time, implying that the pump and probe are pulsed. If the goal is to study carrier dynamics, then the pump must have an energy that can excite electrons from the ground state. Pulsed laser output is typically tuned to an appropriate pump energy via an optical parametric amplifier (OPA) but, as we excited the sample at 400nm, an OPA was unnecessary and, when possible,

second harmonic generation of the laser output (800nm) was produced directly in a BBO crystal. The various types of pump-probe experiment are further differentiated by the type of probe. For example, for a transient absorption measurement the probe is a broadband pulse in the frequency range where the sample absorbs, whereas for a transient photoconductivity measurement the probe will have THz frequency or lower. The temporal resolution of such a measurement is the larger of the width of the pump and probe pulses, so to measure the change in absorption on picosecond timescales, femtosecond pulses are needed. In our case, the (800nm) pulses originate from a Ti:Sapphire laser with a pulse duration of ∼100fs. In this section, we give an overview of transient absorption and terahertz spectroscopies, followed by an overview of relevant kinetics theories.

3.2.1 Transient absorption

The bread and butter of our ultrafast spectroscopy lab is transient absorption spectroscopy, whereby the absorption of a broadband probe is measured with respect to time-after-excitation (delay) (Fig.3.2a). What is actually measured is the intensity of the transmitted probe beam with excitation (T_p) and without excitation (T_0). At a given delay and probe energy, the quantity often reported is the relative change in transmission, calculated as $(T_p - T_0)/T_0$ (Fig.3.2b). However, here we measure the related quantity:

$$ln(T_p/T_0) = ln(e^{-\alpha_p l}/e^{-\alpha_0 l}) \propto \alpha_0 - \alpha_p \equiv -\Delta\alpha, \tag{3.1}$$

where we have simply substituted T_i with Beer's law, with α the absorption coefficient. Since the transmitted intensity gives the number of photons and since every absorbed photon generates one charge pair, a change in transmission directly represents a change in carrier population. Pumping affects absorption simply because transitions which have been excited cannot be excited again. This is known as photobleaching (PB) and results in an increase in transmission, thus resulting in positive $ln(T_p/T_0)$. On the other hand, if an excited carrier can be pumped to an even higher band, then this new photo-induced absorption (PIA) pathway results in a decrease in transmission somewhere in the spectrum, thus resulting in negative $ln(T_p/T_0)$. Lastly, the probe pulse can stimulate emission (SE) from excited carriers, forcing them back to the ground state and resulting in the emission of a photon in phase with the probe pulse, thus resulting in positive $ln(T_p/T_0)$ (Fig.3.2c).

A typical modern TA measurement results in a 2D dataset consisting of probe energy spectrum along one axis and pump-probe delay along the other axis. Slices parallel to the probe energy axis yield spectra typically consisting of summed Gaussians corresponding to distinct carrier populations which can be fitted and tracked over time. Slices parallel to the time axis show population dynamics. An isolated carrier population has an intrinsic decay signature which

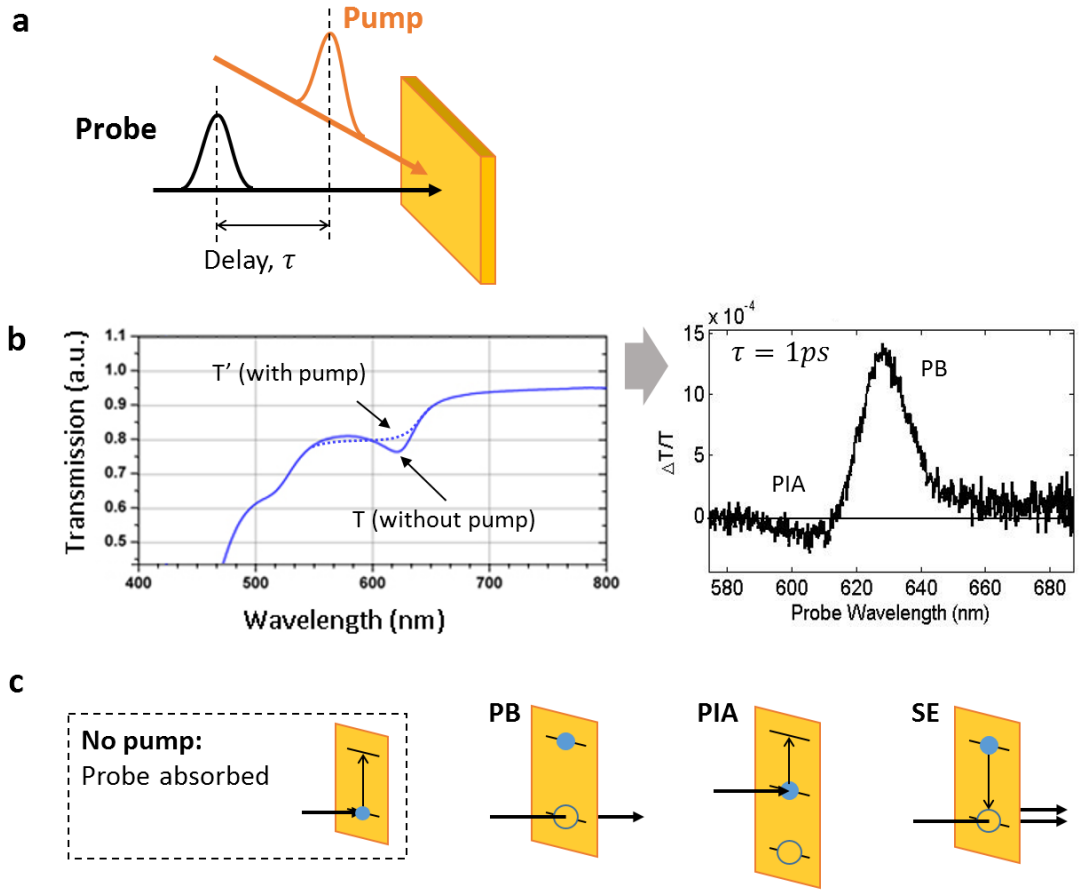

Figure 3.2 (a) Pump and probe pulses are overlapped on the sample, separated in by a temporal delay. The pump excites a transient population, which is subsequently measured by comparing probe transmission with and without the pump. (b)Transient populations are quantified by calculating the relative differential transmission spectrum via $(T_p - T_0)/T_0$ or $ln(T_p/T_0)$, as a function of pump-probe delay τ. This spectrum can be used to identify populations based on their excitation energies. (c) Relative to the no-pumping scenario, photobleaching (PB) and stimulated emission (SE) result in increase in probe transmission, while photoinduced absorption (PIA) causes a decrease in transmission somewhere in the probe spectrum due to a newly-available 2nd excited state.

can be generically expressed as $dn/dt = -k_1 n - k_2 n^2 - k_3 n^3 ...$, where k_i corresponds to an interaction between i carriers (electrons/holes/excitons, depending on the species corresponding to the feature). k_1 represents either recombination of excitons or recombination between a free carrier and a trapped (localized) carrier, k_2 represents bimolecular recombination (including exciton-exciton annihilation), k_3 represents Auger recombination whereby a third carrier absorbs the energy released from a recombination event, and so on (Fig.3.3). When the excitation density is low, the high-order decay channels are eliminated and populations, $n_i(t)$ can be rep-

resented by the master equation formalism, $dn_i/dt = M \cdot n_i$ (Fig.3.4a). This equation represents the exchange of population between multiple carrier states according to a transfer matrix, M (Fig.3.4b). Chapter B (Appendix) depicts how TA might be used to identify charge carrier species in a donor-acceptor system using data simulated via the master equation formalism.

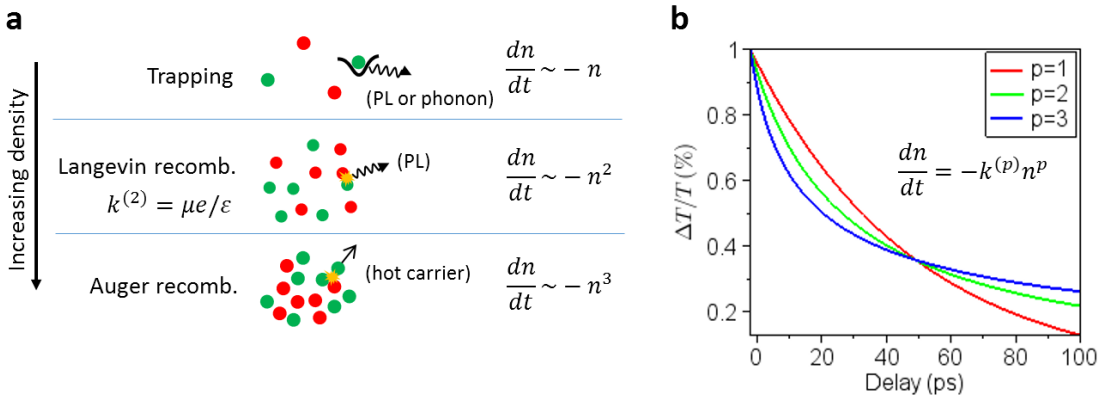

Figure 3.3 (a) When TA spectra are measured over a range of pump-probe delays, cross-sections at a particular probe wavelength represent the population dynamics of all the species contributing to TA signal at that wavelength. If the various species are not interacting, then the dynamics are determined by their respective intrinsic kinetics, which are generally expressed by the equation $dn/dt = -k_1 n - k_2 n^2 - k_3 n^3 ...$ where the term of order p results from interactions between p particles. (b) The qualitative effect of p is shown. When two curves or different kinetic order are fixed at two points, P_1 and P_2, the curve of higher p will decay faster before P_1 and slower after P_2.

We performed TA experiments with a Helios commercial system, crudely diagrammed in Fig.3.5. An femtosecond laser pulse is split into pump and probe paths. The pump beam is tuned with an OPA and chopped mechanically at a rate of 500Hz. The probe pulse is delayed relative to the pump pulse using a mechanical delay stage. The probe beam is then focused to a CaF_2 crystal for white light generation (WLG). Both beams are then focused onto the sample, which is held at 78K in a Janis continuous-flow lN_2 cryostat. When the pump and probe are spatially aligned on the sample and the pump temporally precedes the probe, the probe acquires an additional signal which is either in-phase with probe (increasing transmission) or out-of-phase (decreasing transmission). The transmitted probe is then guided into a fiber-coupled spectrometer, where a grating is used to spectrally separate it onto a CCD which records the spectrum.

The control of the TA experiment involves the syncing of several devices as shown in Fig.3.6. The laser output is pulsed with a repetition rate of 50kHz. The chopper blocks and unblocks

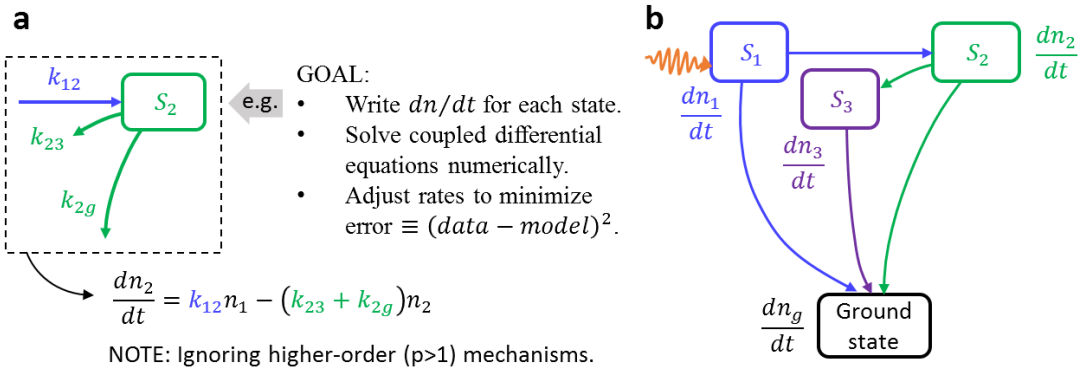

Figure 3.4 (a) When states in a material are interacting (i.e. exchanging population), a system of differential equations (with one dn_i/dt for each population n_i) can be constructed and solved numerically. (b) A diagrammatic representation of the master equation formalism: States connected by rates. Such a system of equations can easily be solved numerically to fit data.

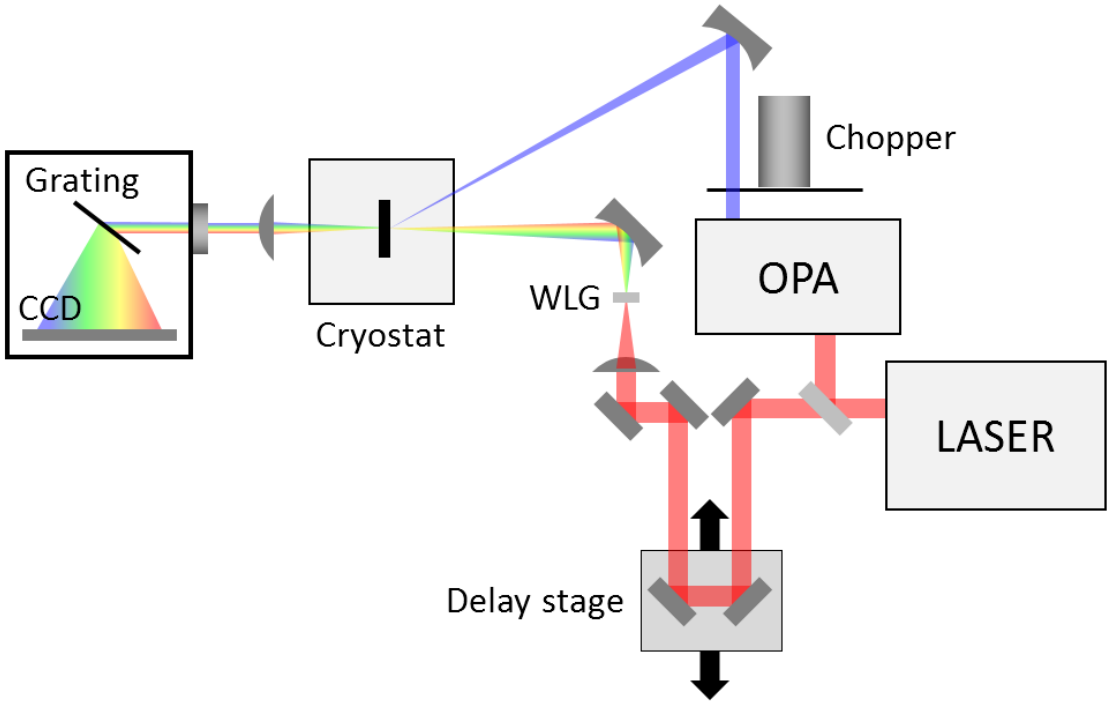

Figure 3.5 Diagram of TA experiment. Output pulse of laser is divided to two pump and probe paths. Pump is tuned by optical parametric amplifier (OPA) and chopped while probe is converted to white light in CaF_2 crystal. Pump excited sample held at low temperature in L-N_2-cooled cryostat, and probe pulse is transmitted after some delay specified by a mechanical delay stage, and is spectrally resolved in a spectrometer-CCD.

the pump at a frequency of 500Hz. Every time the pump is initially blocked (unblocked), the chopper controller triggers the clearing of charge on the CCD, and the probe pulses which subsequently accumulate on the CCD correspond to the T_0 (T_p) spectrum. Alternating T_0 and T_p measurements are performed for 1s at 500Hz. A command is then sent to a delay stage controller which changes the pump-probe delay, and the process is repeated for a list of delays from 0ps to 100ps. The delay is scanned over the entire list multiple times. There are three timescales in the experiment: (1) The pulse scale at which the optical interaction actually occurs at 50kHz, (2) the chopping scale at which alternating T_0 and T_p measurements are performed at 500Hz, and (3) the delay list scale on the order of minutes. At each scale, averaging of N_{rep} repetitions is done which reduces statistical noise at and below the corresponding time scale by a factor of $sqrtN_{rep}$. Furthermore, the first two timescales correspond to point-wise noise in the final dataset, whereas the longest timescale corresponds to slow fluctuations that threaten to distort the shape of the measured dynamics curves.

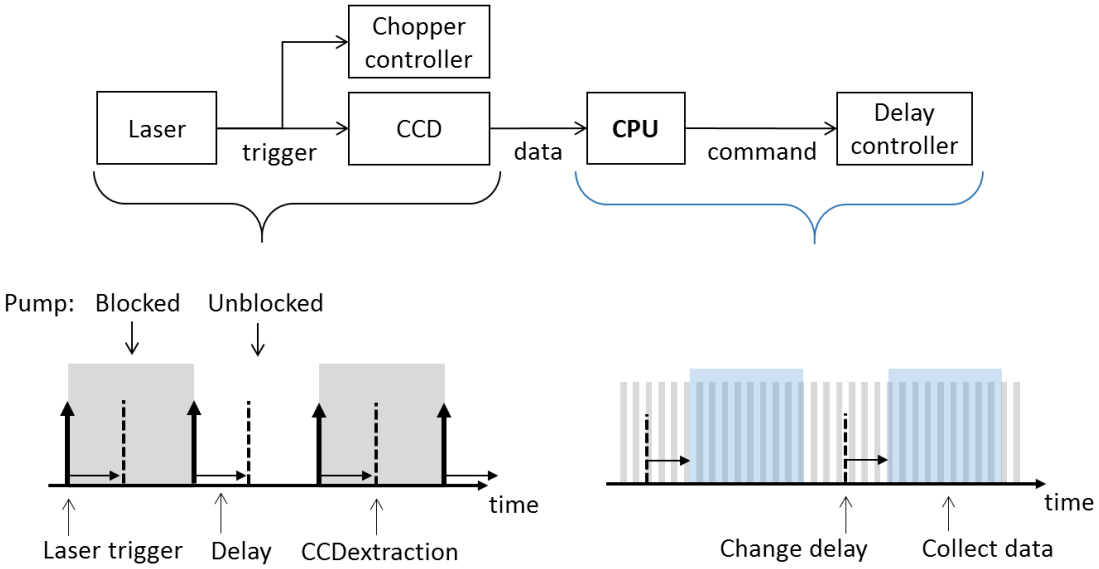

Figure 3.6 Control structure of TA experiment. Chopper and CCD are synced to laser trigger pulse. When chopper state changes, CCD charge is cleared and new collection begins. After some specified delay, CCD extracts charge and reads to computer as either pump-on or pump-off data, which are numerically combined in software. On longer timescales, that software controls the pump-probe delay for each measurement.

3.2.2 Teraherz spectroscopy

Whereas TA uses an optical pump and probe and gives the excited carrier density, the probe in time-domain terahertz spectroscopy (TDTS) is a THz pulse and gives the excited carrier conductivity, a.k.a. photoconductivity $\Delta\sigma$. Because of the high frequency and contactlessness of TDTS, $\Delta\sigma$ constitutes a local measurement of carrier motion free of the limitations and artifacts of device fabrication. $\Delta\sigma$ includes contributions from various forms of carrier scattering. The THz probe allows access to intraband (e.g. excitonic) absorption [41], phonon absorption [42], and carrier scattering mechanisms relevant to conductivity [43] (Fig.3.7a).

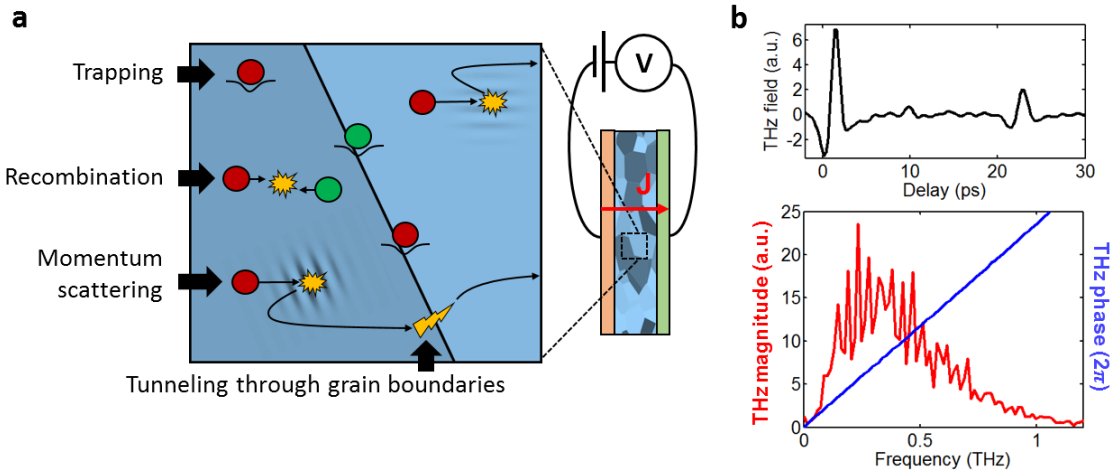

Figure 3.7 (a) Diagrammatic overview of mechanisms affecting macroscopic carrier mobility. (b) Example of the THz pulse used in TDTS with respect to time (top), including an "echo" resulting from back-reflection in the sample, and in frequency-space (bottom), including magnitude oscillations resulting from the aforementioned echo.

Figure 3.8 shows a diagram of the home-built TDTS experiment. Three beams are necessary for the experiment, all of which originate from a Quantronix Integra-C laser with pulse width of 50fs and repetition rate of 1kHz. The THz pulse in our experiment is generated by optical rectification in a ZnTe crystal where, via difference-frequency generation, every mode of the pump is mixed with every other mode. As the bandwidth of the pump is 5nm, difference frequency generation occurs with a peak at around 1THz and a range from 0.2-2THz, corresponding to a pulse with temporal width ∼1ps (assuming Fourier-limited). The THz pulse is detected in another ZnTe crystal via electro-optic sampling, whereby the instantaneous THz field causes the polarization of a secondary 800nm "sampling pulse" to be rotated, with this rotation then being measured with polarization optics and silicon photodiodes. Conveniently, the mathemat-

ics of the sampling pulse measurement is such that the measured intensity after polarization optics is directly proportional to the part of the THz pulse that intersects the sampling pulse in the ZnTe crystal, so the THz pulse shape can then be measured by scanning the delay between these two pulses [44–47] (Fig.3.7b).

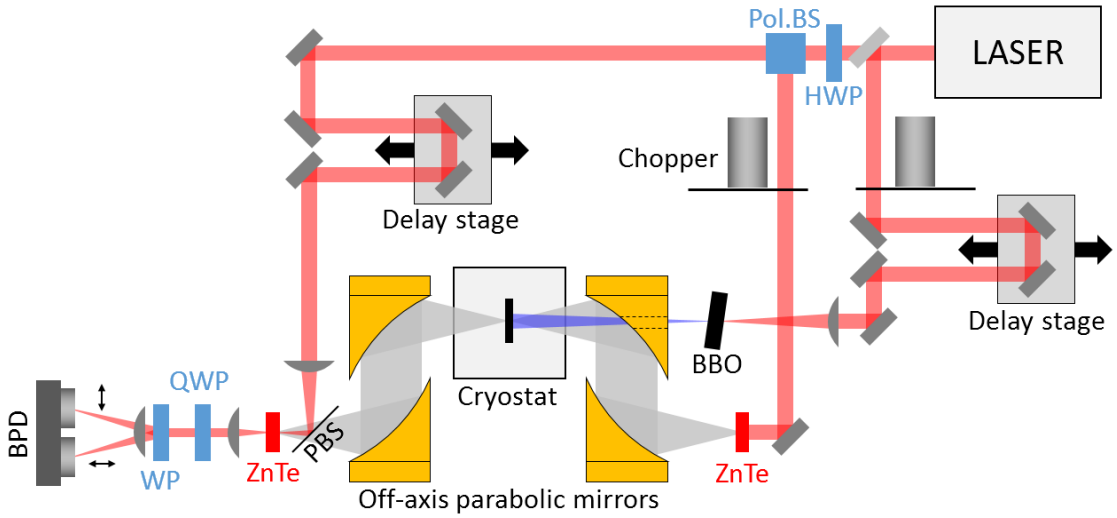

Figure 3.8 Diagram of TDTS experiment. Output pulse of laser is divided into three paths. Two paths are the pump, upconverted to 3.1eV via BBO crystal, and probe, converted to THz range via optical rectification in ZnTe crystal, which are used in pump-probe geometry similar to that of TA experiment. After this, the THz pulse is electro-optically sampled in a ZnTe crystal via the third beam, the polarization of which is then measured with balanced photodetection.

Figure 3.9a shows the control structure of the TDTS experiment. A trigger signal from the laser corresponding to each pulse triggers a Thorlabs chopper controller which is synced so that every other pulse on either the pump or THz path (depending on the mode of operation) is blocked (Fig.3.9b). The chopper rate is measured directly via a built-in light sensor at the base of the chopper, and this rate is sent from the chopper controller to a SRS810 lock-in detector in the form of a reference signal. Meanwhile, the THz experiment is performed, the transmitted THz pulse affects the polarization of the sampling pulse. This effect is detected by splitting the two polarization components of the sampling pulse and measuring their intensity difference with balanced photodiodes (Fig.3.9c). The lock-in detector records this difference into a buffer in real-time. A wave at the frequency of the chopper reference signal is digitally constructed, and the inner product is taken between this wave and the buffered data to extract the modulation of the optical signal (Fig.3.6d), which is induced by the chopper mechanically and by the THz

field electro-optically, and is thus proportional to the THz field strength at the instantaneous moment sampled within the ZnTe crystal. The lock-in detector repeatedly fills a buffer with a real-time length set to 30ms. Matlab is used to interface with both the lock-in detector and the delay stage controller. A command is first sent to the delay stage controller to move to a desired delay and then a value is extracted from the lock-in detector after an appropriate delay proportional to the move time of the delay stage and the real-time length of the lock-in buffer.

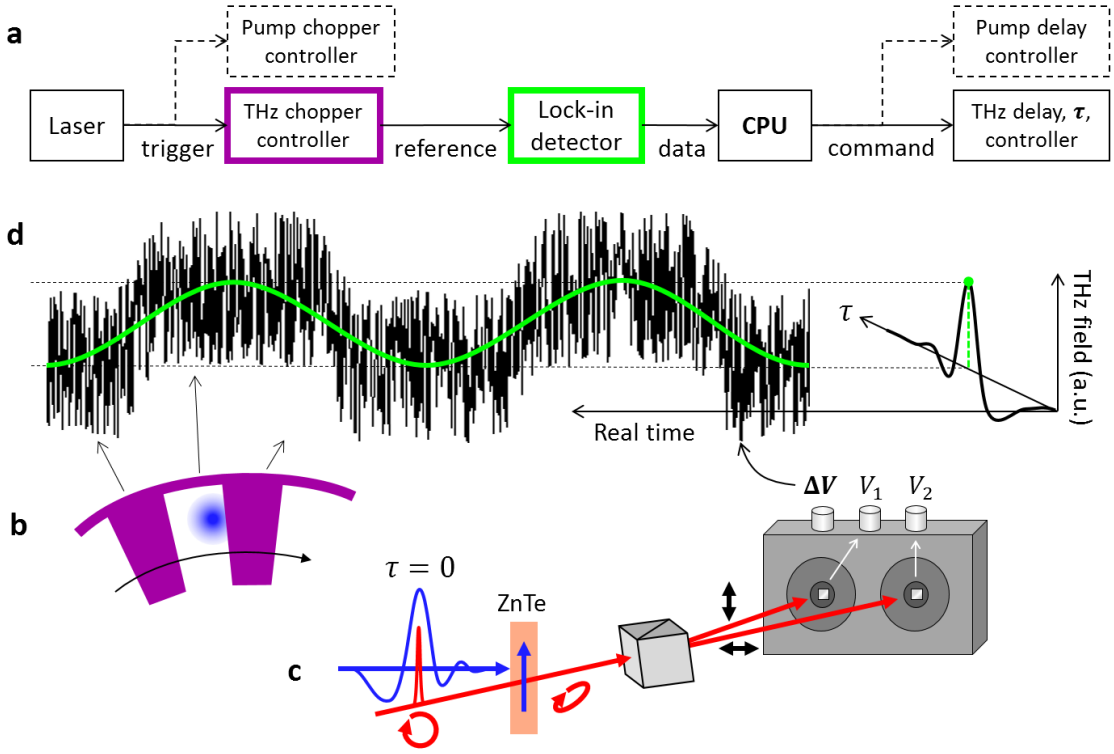

Figure 3.9 (a) Control structure of TDTS experiment, depicting measurement of the THz pulse without no pump or sample. (b) A modulation signature is imparted to the THz beam via mechanical chopping. (c) The THz field at a given point in the waveform rotates the polarization of the sampling beam, and this rotation is measured as a voltage difference between across balanced photodiodes. (d) This voltage difference is read in realtime by the lock-in detector, a component oscillating at the frequency of the chopper is extracted digitally via inner product. The amplitude of this component is proportional to the THz field at the sampled point of the waveform.

When the THz pulse is passed through a material, it's slow field accelerates free (charged) carriers. This driving force is balanced by resistive scattering and reactive restoring forces affecting the carriers, which constitute a conductivity response, $\sigma = J/E$, where σ is related to refractive index $\tilde{n} = \sqrt{2\pi\sigma/i\omega - 1}$ and $\tilde{n}$ determines the output THz pulse via a transfer

function predicted by application of the Fresnel equations (Fig.3.10a). So, these relationships can be used to measure the conductivity of a material by measuring the THz pulse with and without the material (sample) in place, calculating the transfer function, and then using some fitting procedure [48–50] to extract $\tilde{n}$ with the transmission equation given by the Fresnel equations.

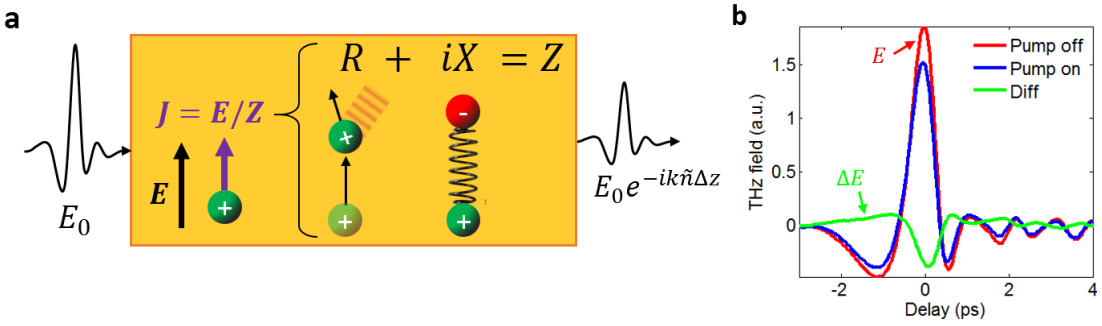

Figure 3.10 (a) The mechanism behind conductivity is the motion of charges in response to a field, $J = \sigma E = E/Z$. The motion of charges can attenuate and shift the transmitted THz field according to the refractive index of the sample, $\tilde{n} = \sqrt{2\pi\sigma/i\omega - 1}$. (b) Since the conductivity can be determined from the transmitted THz field, the change in this transmission due to pumping represents the conductivity of excited charges, $\Delta\sigma$. Only mobile charges respond to the field, so neutral excitons do not contribute to TDTS signal, except for the often-negligible contribution of exciton dipole response. $\Delta\sigma(\omega)$ is calculated from THz transmission and can be fitted by the appropriate conductivity model.

To measure the conductivity of excited carriers, we measure the THz pulse, via electro-optic sampling as previously described, after pumping the material with a femtosecond pump pulse. By changing the delay of the pump pulse, we can then measure $\Delta\sigma$ of free carriers as a function of pump-probe delay. Given the assumption that the measured sample is much thinner than the THz wavelength (which is good for thin films since 1THz corresponds to λ of $0.2mm$) $\Delta\sigma$ can be derived from the Fresnel equation

$$T_\sigma = \frac{2}{1 + \tilde{n}_{sub} + \sigma Z_0/\Delta z} \tag{3.2}$$

$$\Rightarrow \Delta\sigma(\omega) = -\frac{1 + \tilde{n}_{sub}}{Z_0/\Delta z}\frac{\Delta E(\omega)}{E(\omega)}, \quad \frac{\Delta E}{E} \equiv \frac{T_\sigma - T_0}{T_0}, \tag{3.3}$$

where T_σ and T_0 are the THz transmission spectrum with and without pumping, $\tilde{n}_{sub}$ is the refractive index of the substrate, which must be measured separately via the method described previously, Δz is the thickness of the sample, and Z_0 is the impedance of free space. The measured $\Delta\sigma$ can then be fit to an appropriate conductivity model, typically Drude (electron

gas) or Drude-Smith (electron gas + backscattering) [51–53].

A simpler mode of operation for TDTS directly provides dynamics of the integral over the real part of $\Delta\sigma(\omega)$. This is accomplished by simply phasing the sampling pulse to the peak of the THz waveform and measuring pump-probe dynamics at that fixed position. This works based on the principle that the real part of $\Delta E(\omega)$ refers to the cosine terms of $\Delta E(t)$, which have a frequency-independent peak at $t_0 \equiv 0$ (Fig.3.11a). The t_0 point of the sine terms of $\Delta E(t)$ can likewise be associated with the time where the slope is maximized, and thus a 2-point slope can be measured at t_0 as a function of pump-probe delay to extract the integral over the imaginary part of $\Delta E(\omega)$ (Fig.3.11b). As the imaginary part of photoconductivity is associated with bound or confined carriers [41], this technique may allow us to access exciton or trapping dynamics, which are complimentary to free carrier dynamics.

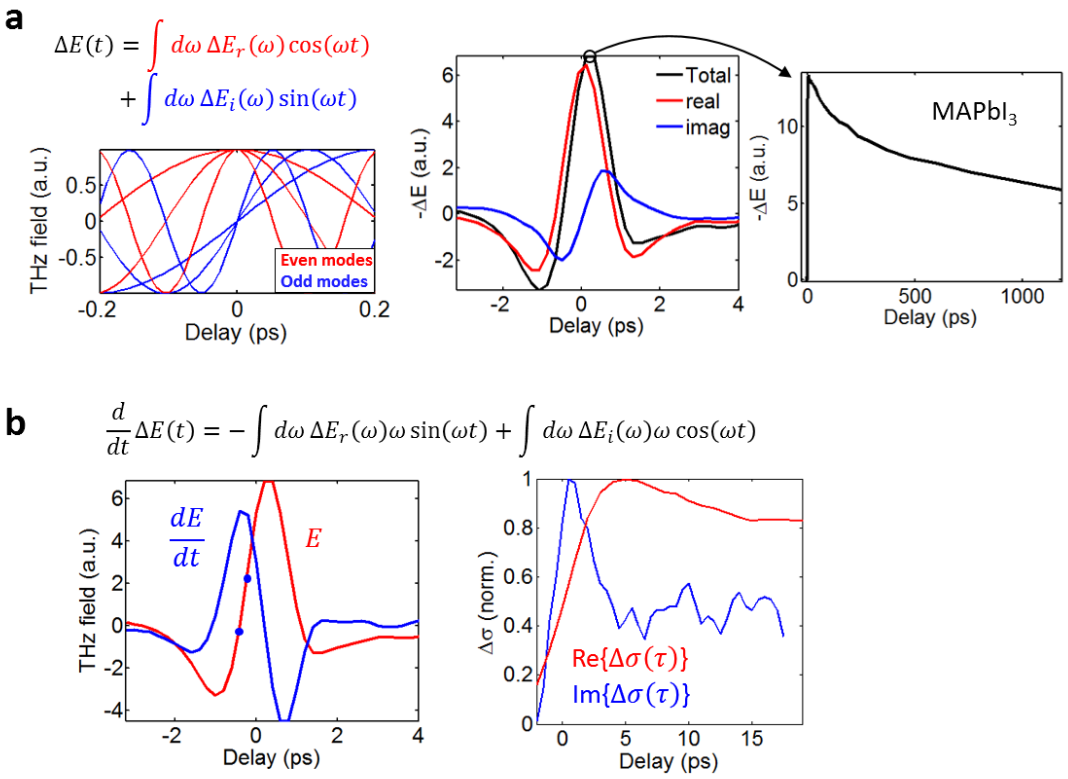

Figure 3.11 (a) The peak value of a function in time, when defined as t=0, represents roughly the integral over the real part of the function in frequency space. This is because the real part is associated with cosine modes, which have a peak at t=0 regardless of frequency. Based on this mathematical principle, a common mode of TDTS is to measure $\Delta E/E \propto \Delta\sigma$ only at the peak of the THz waveform and as a function of pump-probe delay τ. This value is proportional to the integral over the real part $\Delta\sigma$, although the THz spectrum is not actually frequency-resolved. (b) While the μ in $ne\mu$ refers to the in-phase drift velocity of carriers responding to the THz pulse, the dynamics of the out-of-phase motion can be measured via the peak value of the slope of the THz waveform, which corresponds to the integral over the imaginary part of the THz spectrum (weighted toward high ω). In this measurement regime, $\Delta\sigma$ dynamics track the boundness/confinement of carriers. The example on the right shows free carrier formation resulting from exciton decay, via the real and imaginary conductivity dynamics (respectively).

Chapter 4

Research results

4.1 Introduction

Hybrid organic-inorganic perovskites have been a focus of study due to the impressive performance of methylammonium lead iodide ($MAPbI_3$) in photovoltaic (PV) applications, and there has been significant effort invested in optimizing the crystal structure, defect density, and material stability for PV applications. These efforts significantly improved the performance of $MAPbI_3$-based PV performance from 10% to 23% in a short period of time [1, 16, 17]. These studies also triggered research efforts to study perovskites for other device applications. The versatility of the perovskite structure offers great flexibility for tailoring electronic properties to custom functionalities. One of the interesting properties of hybrid perovskites is that they exhibit electronic structural phase transitions as the temperature is changed. Since the electronic properties are tied to material structure, the existence of multiple crystalline phases provide additional flexibility in controlling electronic properties in the material.

$MAPbI_3$ exhibits three different crystalline phases. At room temperature, it is tetragonal (TP). When the material is heated, it transitions to cubic phase at around 310K. When the material is cooled, it transitions to orthorhombic phase (OP) at around 150K. TP and OP exhibit significantly different electronic properties. In TP, the organic cation is freely rotating, allowing it to screen the exciton binding energy [19, 20]. As a result optical excitations quickly form free carriers in TP, which is very useful for high efficiency PV applications. Whereas, in OP, the cation is frozen resulting in excitonic optical transitions. The bandgap of TP is 100meV lower than that of OP. Interestingly, at certain temperatures these two phases can coexist in thin films. As the thin film is cooled below the phase transition temperature, most tetragonal domains become orthorhombic but some remain as tetragonal inclusions in the whole matrix, stabilizing the structure [10]. This coexistence of OP and TP leads to the observation of interesting energy transfer kinetics between the two phases. When the material is optically

excited with photons above the bandgap of OP, photoexcitations quickly transfer into the tetragonal inclusions, prior to radiative recombination. This fast energy transfer process may be interesting for developing new optoelectronic applications using $MAPbI_3$.

At high excitation fluences, when population inversion is achieved, amplified spontaneous emission (ASE) occurs. Basically, spontaneous recombination of carriers stimulates the recombination of other excited sites much like stimulated emission in a laser system. In $MAPbI_3$, when both OP and TP coexist, although OP dominates the material and most carriers are excited in OP, ASE often takes place in TP [3–8]. This property is interesting and makes this system suitable for laser applications. In a process similar to that which sustains lasing in quantum well and quantum dot lasers, carriers injected into OP can then create population inversion and lasing in the lower-energy TP inclusions. In fact Y. Jia et al. [9] found that continuous lasing is achievable with continuous-wave (CW) excitation only from TP and only below the phase transition when the bulk of material is in OP. It is currently believed that these low-energy TP inclusions act as energetic wells which draw in carriers excited in OP, allowing them to reach high concentrations necessary for ASE and, ultimately, continuous lasing. This is a significant step forward for the realization of solution-processed on-chip lasers [54,55]. Continuous lasing under CW excitation is an important first step toward electrically-pumped devices, and yet most organic laser materials cannot sustain CW lasing, instead exhibiting a phenomenon known as lasing death. Therefore the ability to achieve continuous optical gain makes $MAPbI_3$ a promising material for electrically pumped lasing applications.

Although continuous wave lasing from $MAPbI_3$ is observed, the dynamics that lead to lasing have never been studied. Here we studied the ASE phenomenon in $MAPbI_3$ using a comprehensive set of spectroscopy methods including ultrafast transient absorption (TA) and terahertz conductivity (TC). We found that ASE completes within 5ps, and is emitted from unstable excitons after transferring from OP to TP, with ASE death occurring when those excitons dissociate due to screening. Furthermore, we found that the density threshold associated with ASE marks the filling of TP inclusions, with excess OP carriers transferring to TP only after exciton dissociation

4.2 Results

Figure 4.1a shows the steady-state absorption spectrum of $MAPbI_3$ measured as a function of temperature. At room temperature (when material is in TP), no excitonic feature is observed, suggesting that optical excitation of TP results in free carriers [22,23]. This is typical of materials where the exciton binding energy is on the order of the available thermal energy k_BT (25meV at room temperature), TP excitons having a binding energy that is estimated to be 10meV [12, 19, 56]. However an excitonic feature appears as the temperature is lowered near the phase

transition from TP to OP at 150K and is large in OP absorption below the phase transition, suggesting that absorption results in excitons in OP. Based on absorption data, the phase transition appears to be complete, with the TP band edge completely disappearing below 140K.

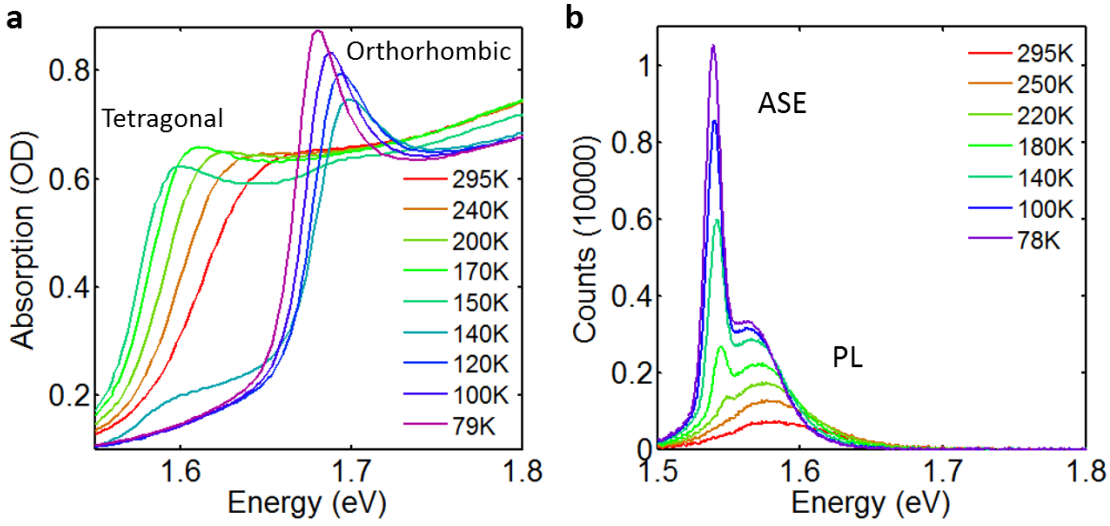

Figure 4.1 (a) Absorption spectra of $MAPbI_3$ from 295K to 79K, showing the phase transition from TP to OP at 150K. (b) Emission spectra of over the same temperature range, showing PL at 1.56eV and narrow ASE appearing at 1.53eV as temperature is lowered.

Figure 4.1b shows emission measured as a function of temperature. The excitation source is a 3.1eV 9μJ/cm^2 ultrashort laser pulse. The spectrum shows two features: A broad PL band at 1.56eV (hereafter referred to simply as "PL") resulting from spontaneous recombination of carriers at the TP band edge, and a narrow ASE band at lower energy. As temperature is lowered, PL becomes narrower due to decreased thermal broadening, and redshifts due to decreased electron-phonon coupling [57]. Both of these effects result in quenched non-radiative recombination and increased mobility, which in turn contribute to increased PL and ASE.

To study ASE behavior further, we measure emission as a function of excitation fluence at 78K where ASE efficiency is maximized (that is, within the temperature range achievable via L-N_2 cooling). Spectra are shown in Fig.4.2a, with fluence reported based on the resulting excitation density, the number of absorbed photons per volume (SI.A.1). ASE appears at an excitation density of $10^{18} cm^{-3}$, similar to previous reports [58].

As ASE rises up, PL begins to saturate. This apparent decrease in PL efficiency has been previously attributed to the onset of Auger losses [4], which are expected to occur at high

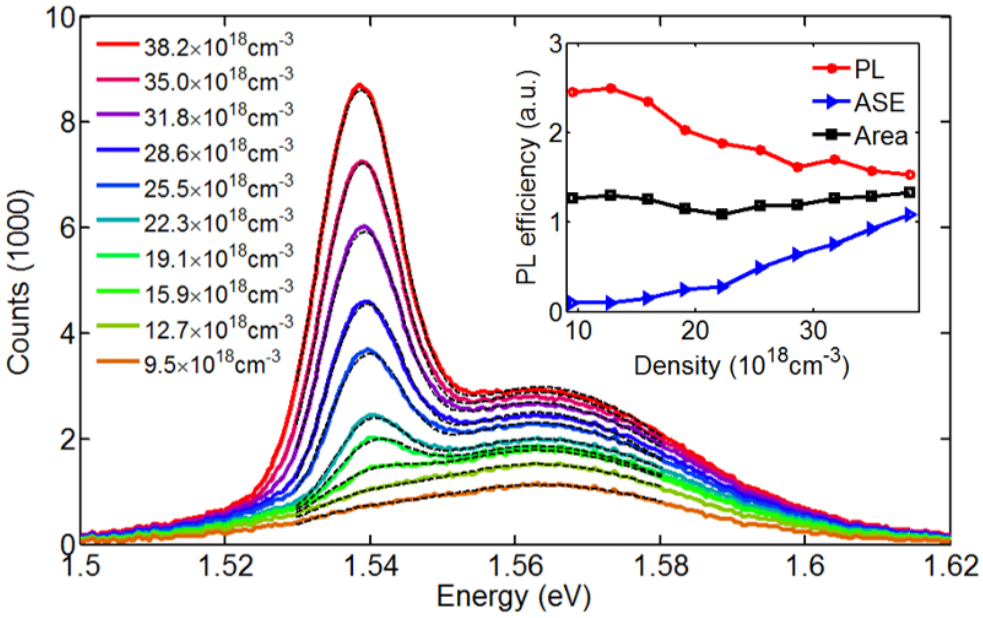

Figure 4.2 Emission over a range of excitation densities, showing ASE appearing at around $10^{18} cm^{-3}$. Two-Gaussian fittings (black dashed) are performed, and the efficiency (calculated area divided by excitation density) for each feature versus excitation density is shown in the inset, along with the total efficiency calculated from the area under the emission curve divided by excitation density.

density. To explore this possibility, we perform Gaussian fittings on the PL and ASE features and calculate the emission efficiency for each as a function of excitation density, and also numerically calculate the area under the entire PL spectrum. ASE efficiency increases with excitation density while PL efficiency decreases, and the overall efficiency (total area divided by excitation density) remains fairly flat with the exception of a small dip at the excitation density where ASE appears. Increasing excitation density affects the branching ratio between PL and ASE, and this suggests that ASE occurs before PL, essentially outcompeting it. This explains why PL ceases to increase much after excitation density exceeds the ASE threshold. Nonradiative Auger recombination is also expected to take effect at high densities, so the fact that emission efficiency does not experience an appreciable decrease with increasing excitation density suggests either that we are still below the Auger recombination threshold or that ASE is a faster process than Auger recombination.

We also measure PL and ASE lifetimes via time-correlated single photon counting (Fig.4.2b). ASE is nearly completed within the instrument response time (1ns) whereas PL is much slower. As this measurement cannot resolve the timescale on which ASE apparently occurs (<1ns), measurements with higher time resolution are necessary to study ASE. To probe ultrashort timescales on the order of picoseconds, we use TA.

TA gives information about absorption dynamics of carrier populations. A 3.1eV pump pulse excites the sample and, after some delay τ, a broadband probe pulse is transmitted and spectrally resolved using a spectrometer (T_p). The probe transmission is also measured with no pumping at all (T_0). $ln(T_p/T_0)$ is measured as a function of pump-probe delay. All TA experiments were performed with the sample at 78K. We measure TA over a range of excitation densities, starting below the ASE threshold at $1.5 \times 10^{18} cm^{-3}$ and going up to $38 \times 10^{18} cm^{-3}$ where strong ASE was observed.

Figure 4.3a shows TA spectra for excitation below the ASE threshold, from 0ps pump-probe delay (immediately after excitation) to 100ps. The spectral shape changes drastically up to 2ps and is static after that. From their spectral locations, we attribute the positive 1.6eV and 1.7eV peaks to photobleaching of TP and OP, respectively (PB_T and PB_O). To identify features associated with stimulated emission (and presumably also ASE), in Fig.4.3b we compare TA at early and late delay with the emission spectrum showing PL and ASE (including an atypical spectrum showing ASE from OP). OP ASE aligns with the narrow TA feature at 1.63eV, which we thus label SE_O. Likewise, we label the narrow TA feature at 1.53eV as SE_T. There are broad negative photo-induced absorption (PIA) features at 1.57eV at early delay and 1.5eV at late delay. These energies correspond to PB_O and PB_T redshifted by $\sim$100meV, so we label these features PIA_O and PIA_T, respectively. This redshifted absorption has been observed previously and was attributed to excitons [22, 59, 60] and bandgap renormalization due to unscreened interactions [20].

Having identified SE_T, which presumably will exhibit an ASE signature, in Fig.4.4 we focus on the dynamics of SE_T at 1.535eV as a function of excitation density, in order to observe the threshold and dynamics of ASE. At low excitation density, PIA_O decays within 1ps and is replaced by slowly-decaying SE. As excitation density is increased, the slow SE saturates and a fast component appears at $7 \times 10^{18} cm^{-3}$. This behavior is reminiscent of the ASE and PL in the emission spectra in Fig.4.2a, and thus we attribute the fast SE_T decay components to ASE.

The sudden death of ASE after 6ps suggests that the TP population has been depleted to below the ASE density threshold. To see what is going on elsewhere in the system, in Fig.4.5a we consider TA spectra for the highest excitation density studied, well above the ASE threshold, from 0ps to 100ps delay. Unlike below the ASE threshold, where PB_O decays within 1ps, at high excitation density PB_O remains for much longer. It finally starts decaying at 6ps, after ASE completes. In Fig.4.5b we look at the dynamics of PB_O at 1.68eV as a function of excitation density. Below the ASE threshold, OP population rises up and decays immediately within 2ps as excitons transfer to TP. Above the ASE threshold, OP population rises up and then decays down to a plateau, suggesting that TP inclusions have been filled and the remaining OP excitons cannot transfer. While the initial transfer rate appears to have no dependence on excitation density, the number of carriers remaining in OP (indicated by the height of the

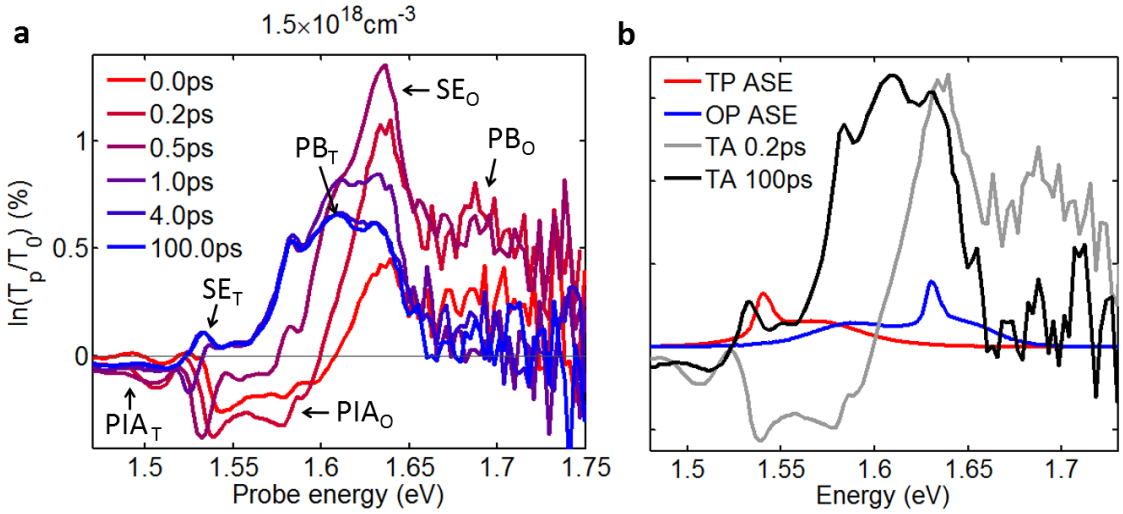

Figure 4.3 (a) TA spectra for $1.5 \times 10^{18} cm^{-3}$ excitation density, for various pump-probe delays. Annotations label the features as they are identified in the main text. (b) Comparison of early-delay (gray; OP-dominated) and late-delay (black; TP-dominated) TA spectra and two emission spectra showing ASE from TP (red) and OP (blue). OP ASE and PL were observed only occasionally throughout our studies, and may be quenched by repeated temperature cycling (see SI.A.2).

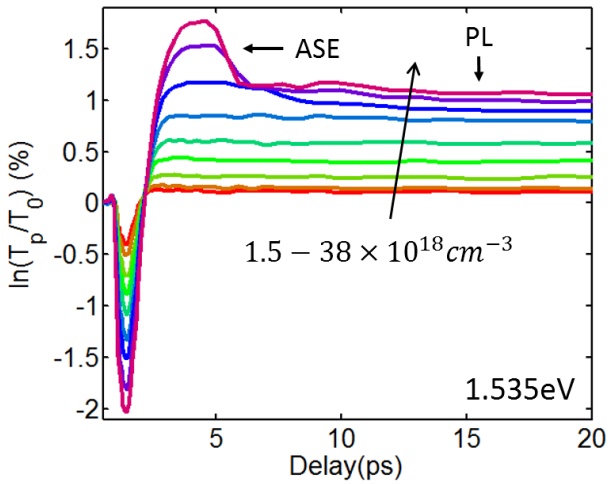

Figure 4.4 TA dynamics at the energy associated with SE_T as a function of excitation density. At the ASE threshold found for steady-state measurements, a TA component appears, which we associate with ASE completing within 5ps. The initial negative component is PIA_O, which decays immediately upon the initial transfer of carriers from OP to TP.

plateau) increases above the ASE threshold.

So far, we have found that ASE occurs from TP carriers in the 3-6ps time period, but we have been unable to say whether these carriers are free or excitonic. To probe the nature

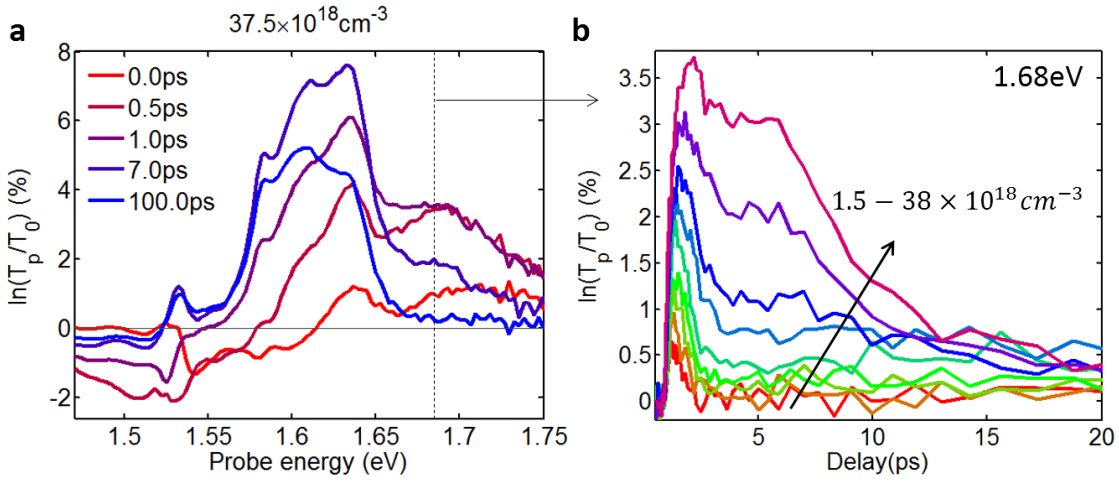

Figure 4.5 (a) TA spectra for $38 \times 10^{18} cm^{-3}$ excitation density, for various pump-probe delays. OP population is relatively long-lasting when excitation density is above ASE threshold. (b) Dynamics of PB_O, showing initial carrier transfer to TP, followed by a plateau during the ASE period, followed by final decay of OP population.

of these carriers, we measure time-resolved terahertz conductivity (TC) dynamics. Just as for emission and TA experiments, we excite the sample with an ultrashort 400nm pump pulse. TC dynamics are reported as the relative change of the transmitted THz probe, $\Delta E/E \propto \Delta\sigma$ where $\Delta\sigma$ is the photoconductivity of excited carriers. Measuring this quantity at the peak of the THz waveform gives the integral over the real part of the photoconductivity (hereafter referred to as Re(TC)), given by Re(TC)$= ne\mu$ where n is population density of free carriers, μ is mean AC mobility, and e is electron charge. Thus we can measure dynamics of conductive free carriers by simply monitoring this peak value while scanning pump-probe delay. Figure 4.6a shows a survey of Re(TC) dynamics at 180K, 140K, and 78K. At 180K, Re(TC) rises immediately and decays with slow monotonic dynamics. A fast decay component emerges as the temperature is lowered. When excitation density is increased (Fig.4.6b), this fast decay component increases while the slow decay component saturates. This saturation behavior suggests that the faster decay mechanism is outcompeting the slower one at high densities, reminiscent of the behavior previously observed at the ASE threshold.

To compare this feature to the behavior observed in TA, we look closer at the fast Re(TC) decay component at 78K about the ASE threshold (Fig.4.6c). The fast Re(TC) decay appears at an excitation density of $4 \times 10^{18} cm^{-3}$, similar to the ASE threshold observed in emission and TA experiments. Signal rises in 3ps, and the fast component decays within 10ps to the level of the remaining slow component, which appears to saturate at excitation densities above the ASE threshold.

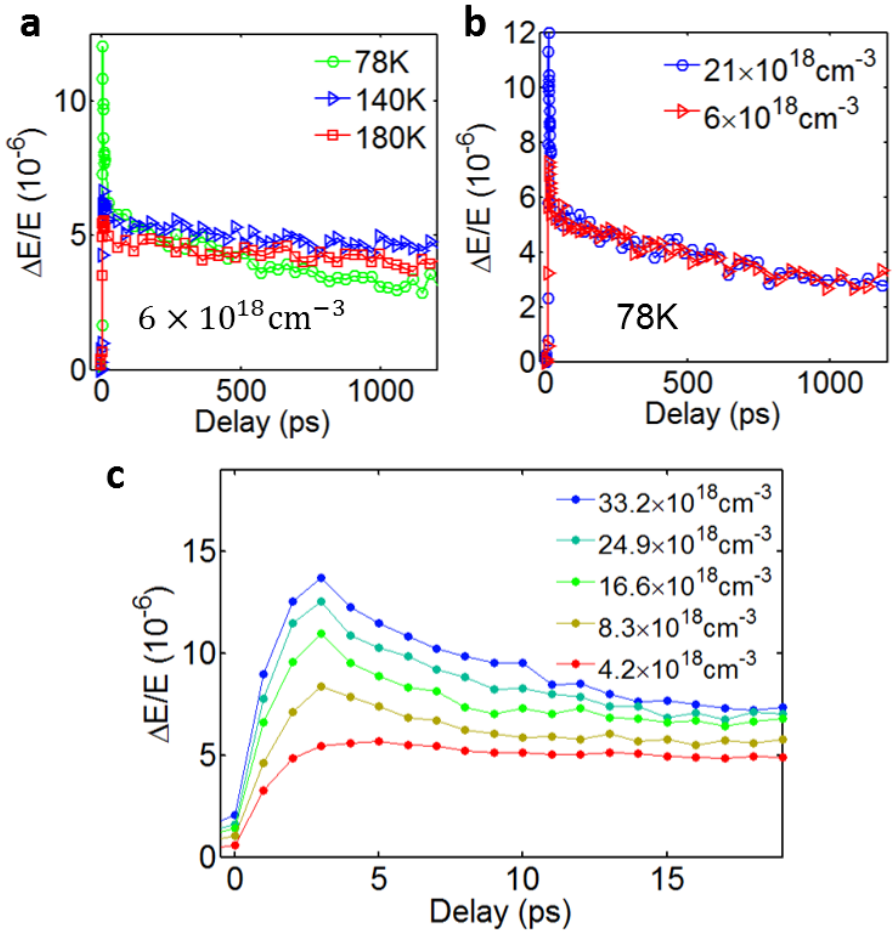

Figure 4.6 (a) Re(TC) dynamics for $6 \times 10^{18} cm^{-3}$ excitation density and from 78K to 180K, showing the appearance of a fast component at low temperature. (b) Re(TC) dynamics at 78K and at excitation densities of $6 \times 10^{18} cm^{-3}$ and $21 \times 10^{18} cm^{-3}$. The fast component increases while the slow component remains the same. (c) Focus on the fast Re(TC) component over a range of excitation densities from ASE threshold and upward.

The 10ps free carrier decay is similar to the 10ps PB_O decay observed at high excitation density in the TA data. Free carrier formation still takes several picoseconds, about as long as it takes for ASE completion according to TA. Therefore it may be that ASE precedes free carrier formation, and that in fact the ASE period is terminated by exciton dissociation. As excitons are bound carriers, they are unable to respond in-phase to a field, and so have no real response toward the low-frequency limit. However, bound carriers can respond out-of-phase to the THz field, and the resulting frequency-integrated imaginary TC, Im(TC), can be extracted from the peak value of the derivative of $\Delta E/E$, as a function of pump-probe delay. Im(TC) dynamics at excitation density of $33 \times 10^{18} cm^{-3}$ are shown in Fig.4.7a, alongside Re(TC) dynamics at the same excitation density. We observe a fast decay component, which rises within the instrument response time and decays within 5ps while Re(TC) is still on the rise. This decay is followed by an oscillating component which is otherwise constant (Fig.4.7b).

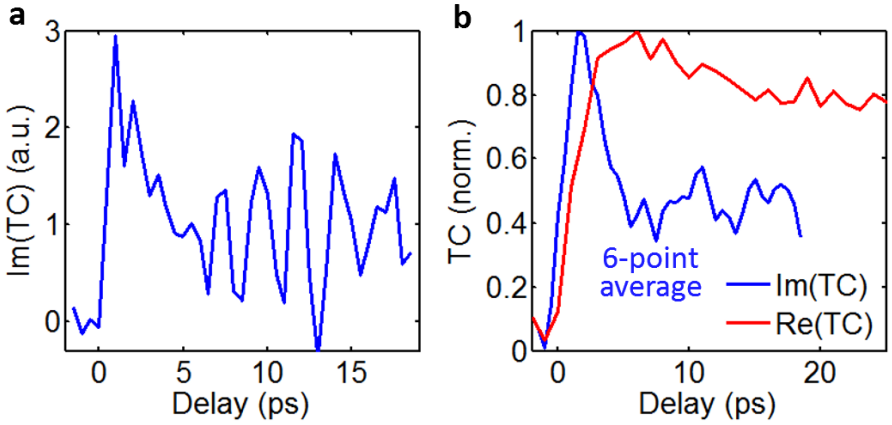

Figure 4.7 (a) Im(TC) dynamics for $33 \times 10^{18} cm^{-3}$ excitation density, showing fast decay followed by large oscillations. (b) Comparison of Re(TC) (red) and Im(TC) (blue; smoothed with 6-point window), both at $33 \times 10^{18} cm^{-3}$ excitation density. Fast Im(TC) decay presumably represents exciton dissociation, and corresponding free carrier formation is represented by the relatively slow rise of Re(TC).

4.3 Discussion

We found that PL is emitted from TP over the entire range of temperatures studied (and for the vast majority of trials; see SI.A.2), despite absorption data implying that a complete phase transition from OP to TP occurs at 150K. This apparent contradiction between absorption and emission has been previously observed and is attributed to TP inclusions remaining below the

phase transition temperature, and being the primary emitter while accounting for only a small fraction of the total volume [10]. The simultaneous strong absorption in OP and emission from TP suggests fast carrier transfer from OP to TP at a rate that is much faster than the intrinsic decay rate of the OP excitons [23, 61]. We find the transfer of carriers from OP to TP to occur within 2ps according to the initial PB_O decay. Transfer is complete below the ASE threshold, but is halted at excitation densities above the ASE threshold when TP inclusions become filled. These static PB_O standby carriers prove that the intrinsic decay rate of OP carriers is negligible compared to the rate of transfer from OP to TP at low excitation density.

The transfer of carriers from OP to TP is marked by the sharp initial decay of PB_O as well as the decay of the broad PIA feature at around 1.58eV on the same timescale. If the PIA corresponds to redshifted absorption due to bandgap renormalization, then the fact that PIA_T is much weaker than PIA_O is consistent with the much higher dielectric constant in TP relative to OP. The dielectric constant in TP is so large in part because of screening due to rotation of the organic cation [12, 19]. The orientation of this cation has been found to have a response time of a few picoseconds [31]. This is the time it takes for an exciton in TP to invoke the full dielectric screening response of the environment. Therefore the fast initial decay of Im(TC) may correspond to the dissociation of excitons due to screening. Furthermore, as this exciton dissociation appears to be correlated with the end of the ASE period according to SE_T dynamics, we assert that ASE is emitted from TP excitons. This proposed mechanism is consistent with the longer 100ps ASE lifetime observed in $CsPbBr_3$ [62], which is unable to screen via cation rotation.

As the exciton population is decaying according to Im(TC), free carrier formation occurs according to the rise of Re(TC). In the 6-20ps time range after ASE death, free carrier population decays. In TA spectrum (Fig.4.8a), we see that this decay is isolated to PB_O and SE_O, and thus we attribute the loss of free carrier population represented by Re(TC) decay to decay of the remaining OP population. While the overlap between OP and TP features makes it hard to separate their individual contributions around the middle and upper part of PB_T, at the low-energy side of PB_T at 1.56eV, we see a rise with time constant close to that of OP population decay. This suggests that the remaining OP population is transferring to TP during this period starting at ASE death. Thus the decaying Re(TC) may be indicative of the decrease in mobility of free carriers as they transfer from OP to TP, due to cationic scattering in TP.

Figure 4.9 shows a comparison of TC data and TA data at spectral positions previously used to represent OP (1.68eV) and TP (1.56eV) populations. While Re(TC) is decaying from 6-20ps in accordance with the transfer of carriers from OP to TP, Im(TC) remains fairly flat. The lack of a corresponding decay of Im(TC) during this time period means that OP excitons have also completely dissociated at this point, suggesting that OP excitons may be screened at the OP-TP interface. The lack of an Im(TC) decay after ASE death also indicates that these

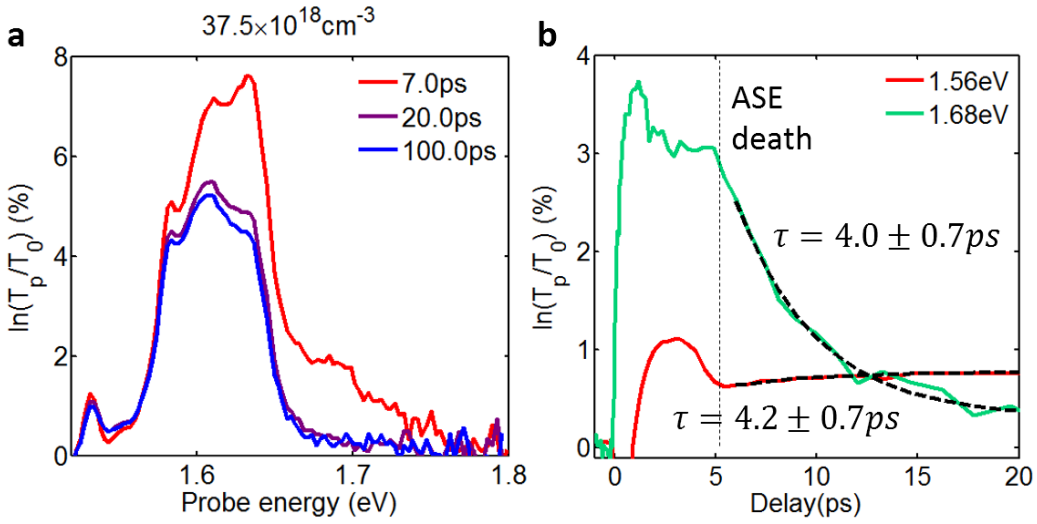

Figure 4.8 (a) TA spectra for $33 \times 10^{18} cm^{-3}$ excitation density and after ASE death, showing the remaining OP population, represented by SE_O and PB_O, decaying within 20ps after excitation. (b) TA dynamics at 1.56eV and 1.68eV corresponding to TP and OP population, respectively, with fitting showing similar lifetime (95%CI). TP population dynamics are taken at the very bottom of PB_T, where contribution of SE_O and PB_O are minimal, though the contribution of SE_T can be seen at early delay.

remaining OP free carriers have a totally real conductivity response. This is very different from the conductivity response of TP carriers, which is represented by the flat component of Re(TC) and Im(TC) remaining after 20ps when transfer is complete. The mix of real and imaginary conductivity response of TP carriers is indicative of the popular Drude-Smith model, which is essentially the Drude model modified by a 2nd-order expansion term often attributed to backscattering [18, 43, 51, 63]. The slow transfer of OP free carriers after ASE death, compared to the initial fast transfer of OP excitons within 2ps, may be due to Coulombic scattering at the OP-TP interface which would affect charge-neutral excitons less. Such Coulombic scattering may result from ion migration resulting in the accumulation of ions at the interface [64–66].

While there is the ability to tune the bandgap and other electronic properties in HOIP-based lasers via chemical substitution, much of the recent focus has been on tuning the photonic environment, bridging the gap between ASE and lasing by producing various resonator geometries through microstructure. These have included colloidal nanocrystals, hexagonal crystals decorated with spherical resonators, nanorods, and microdisks [6, 7, 67–69], to name a few. It has also been found that thermal gradients can be used to induce spontaneous periodic micro-arrays upon crystal growth with low trap density and very strong ASE [15]. In using microstructure to hone the ASE output, these discoveries are promising for future applications in on-chip lasers. Thus we can say the same for the special structure that emits ASE at low temperature in

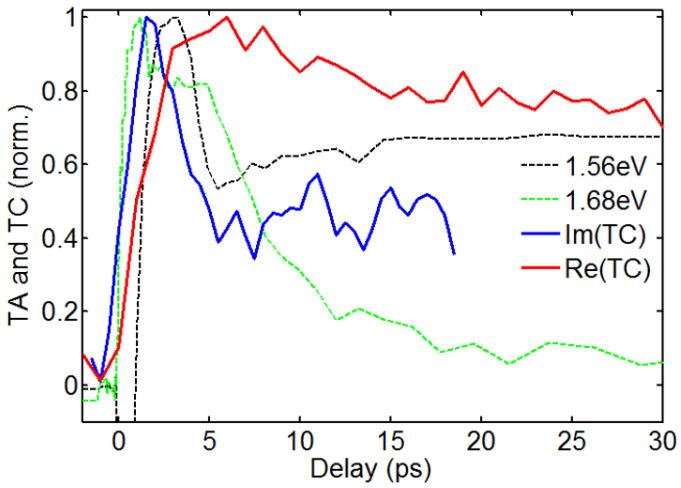

Figure 4.9 TA cross sections in Fig.4.8b compared to Re(TC) and Im(TC). At late delay (>20ps) OP population goes to zero while TP population is constant. This allows us to identify The Re(TC) decay with OP carriers, and the late-delay components of Re(TC) and Im(TC) with TP carriers. The fast Im(TC) decay and Re(TC) rise correspond to exciton dissociation.

$MAPbI_3$ (TP inclusions in an OP matrix). In this operation regime, carrier concentration upon transfer to TP inclusions offers the possibility of continuous lasing at extremely low thresholds, and thus with very high power efficiency [9, 58]. While these findings have helped to clarify the effect of microstructure on ASE efficiency and sustainability, there have been no prior ultrafast temporal studies of the inter-phase transfer resulting in ASE, or of the ASE process itself, as far as we know. Our contribution shows that ASE occurs on an extremely short timescale of a few picoseconds, suggesting applications in ultrafast optical switches and amplifiers. The timescale of ASE is determined by two things: (1) The filling of TP inclusions which takes only 2ps, and (2) exciton dissociation which takes a few picoseconds. On the first factor, the filling time presumably depends on the size and occurrence of TP inclusions. These properties are dependent on temperature and can also be permanently affected by temperature cycling [65], but they may also depend on the $MAPbI_3$ microstructure under study. The transfer leading to ASE can be studied with ultrafast measurements similar to those used here in order to determine if there is a relationship between microstructure and the properties of TP inclusions at low temperature. On the second factor, as ASE is apparently quenched upon exciton dissociation, further work in this direction can attempt to control the bandwidth of ASE through chemical substitutions aimed at tuning exciton lifetime in the OP and TP phases.

4.4 Conclusion

In summary, we have performed comprehensive power-dependent ultrafast studies of $MAPbI_3$ at low temperature. In TA spectra, we identified a feature associated with ASE based on the similar power-dependence and spectral position of ASE in steady-state emission. This allowed us to determine that ASE is emitted from TP inclusions within the first 5ps after excitation. We tracked OP and TP populations, and found that excitons excited in OP transfer to TP inclusions within 2ps. The ASE threshold corresponds to the excitation density sufficient to fill TP inclusions, leaving some surplus carriers in OP. After this filling is complete, ASE at 1.53eV is emitted from TP excitons while excitons in both OP and TP rapidly dissociate. This dissociation completes after 5ps, resulting in ASE death. The remaining OP free carriers transfer to TP inclusions rather slowly compared to the initial transfer, presumably due to Coulombic scattering by accumulated ions at the OP-TP interface.

The ultrafast ASE quenching effect observed here may be useful for certain applications such as in ultrafast pulse conversion, whereby a material with a customized bandgap is used to convert the energy of an ultrashort laser pulse into a Stokes-shifted ASE pulse. To take advantage of the exciton/ASE quenching effect at room temperature, $MAPbI_3$ can be embedded in a material designed to have high exciton binding energy and high bandgap relative to TP, in order to encourage exciton transport and thus ASE. For pulse conversion applications, short ASE pulses require TP inclusions to be small, while high power requires them to be big, so there will be an inevitable trade-off between bandwidth and power.

4.5 Methods

$MAPbI_3$ samples were provided by David Mitzi, and were synthesized via solution processing techniques. Samples consisted of a 1in×1in×1mm glass substrate, with a ∼500nm spin-coated $MAPbI_3$ layer. Low temperature measurements were performed in a Janis continuous-flow lN_2 cryostat. The laser used for PL and TC is an Integra-C Ti:Sapphire laser with 50fs pulsed output at 800nm. PL was collected in a Mightex spectrometer. TC was measured with a homebuilt TDTS system. THz pulses were generated in a ZnTe crystal and with spectral range from 0.2-2THz. The transmitted THz beam was detected via electro-optic sampling in ZnTe, and balanced detection of the resulting polarization shift. TA experiments were performed in a commercial Helios system, with pump and probe originating from a Libra regenerative amplifier. The pump was produced with a Coherent OPerA Solo and the white light probe was generated with a CaF_2 crystal. Delay for all ultrafast experiments was produced with Newport mechanical delay stages.

BIBLIOGRAPHY

[1] M. M. Lee, J. Teuscher, T. Miyasaka, T. N. Murakami, and H. J. Snaith. Efficient hybrid solar cells based on meso-superstructured organometal halide perovskites. *Science*, 338, 2012.

[2] C. Wehrenfennig, G. E. Eperon, Michael B. Johnston, H. J. Snaith, and L. M. Herz. High charge carrier mobilities and lifetimes in organolead trihalide perovskites. *Adv. Mater.*, 26, 2014.

[3] E. Lafalce, C. Zhang, Y. Zhai, D. Sun, and Z. V. Vardeny. Enhanced emissive and lasing characteristics of nano-crystalline mapbbr3 films grown via anti-solvent precipitation. *J. Appl. Phys.*, 120, 2016.

[4] M. Cadelano, M. Saba, N. Sestu, V. Sarritzu, D. Marongiu, F. Chen, R. Piras, F. Quochi, A. Mura, and G. Bongiovanni. Photoexcitations and emission processes in organometal trihalide perovskites. *InTech*, 12, 2016.

[5] F. Yuan, Z. Wu, H. Dong, B. Xia, J. Xi, S. Ning, L. Ma, and X. Hou. Electric field-modulated amplified spontaneous emission in organo-lead halide perovskite ch3nh3pbi3. *Appl. Phys. Lett.*, 107, 2015.

[6] B. Yang, X. Mao, S. Yang, Y. Li, Y. Wang, M. Wang, W. Deng, and K. Han. Low threshold two-photon-pumped amplified spontaneous emission in ch3nh3pbbr3 microdisks. *ACS Appl. Mater. Interfaces*, 8, 2016.

[7] S. Yakunin et al. Low-threshold amplified spontaneous emission and lasing from colloidal nanocrystals of caesium lead halide perovskites. *Nat. Comm.*, 6, 2015.

[8] L. Qin, L. Lv, C. Li, L. Zhu, Q. Cui, Y. Hu, Z. Lou, F. Teng, and Y. Hou. Temperature dependent amplified spontaneous emission of vacuum annealed perovskite films. *RCS Adv.*, 7, 2017.

[9] Y. Jia, R. A. Kerner, A. J. Grede, B. P. Rand, and N. C. Giebink. Continuous-wave lasing in and organic-inorganic lead halide perovskite semiconductor. *Nature Photonics*, 11, 2017.

[10] C. Wehrenfennig, M. Liu, H. J. Snaith, M. B. Johnston, and L. M. Herz. Charge carrier recombination channels in the low-temperature phase of organic-inorganic lead halide perovskite thin films. *APL Mater.*, 2, 2014.

[11] K. Galkowski et al. Spatially resolved studies of the phases and morphology of methylammonium and formamidinium lead tri-halide perovskites. *Nanoscale*, 9, 2017.

[12] J. M. Frost, L. D. Whalley, and Aron Walsh. Slow cooling of hot polarons in halide perovskite solar cells. *ACS Energy Lett.*, 2, 2017.

[13] T. Numai. *Fundamentals of semiconductor lasers*. Springer-Verlag New York Inc., 2004.

[14] Y.-S. Park, W. K. Bae, T. Baker, J. Lim, and V. I. Klimov. Effect of auger recombination on lasing in heterostructured quantum dots with engineered core/shell interfaces. *Nano Lett.*, 15, 2015.

[15] N. Cho et al. Pure crystal orientation and anisotropic charge transport in large-area hybrid perovskite films. *Nat. Comm.*, 7, 2016.

[16] Z. Shi and A. H. Jayatissa. Perovskites-based solar cells: A review of recent progress, materials and processing methods. *Materials*, 11, 2018.

[17] Nrel: Best research cell efficiencies. https://www.nrel.gov/pv/assets/pdfs/pv-efficiencies-07-17-2018.pdf. Accessed: 2018-10-08.

[18] C. S. Ponseca Jr. and V. Sundstrom. Revealing the ultrafast charge carrier dynamics in organo metal halide perovskite solar cell materials using time resolved thz spectroscopy. *Nanoscale*, 8, 2016.

[19] J. Even, L. Pedesseau, and C. Katan. Analysis of multivalley and multibandgap absorption and enhancement of free carriers related to exciton screening in hybrid perovskites. *J. Phys. Chem. C*, 118, 2014.

[20] M. T. Trinh, X. Wu, D. Niesner, and X.-Y. Zhu. Many-body interactions in photo-excited lead iodide perovskite. *J. Mater. Chem. A*, 3, 2015.

[21] F. Bertoletti et al. Coherent nanotwins and dynamics disorder in cesium lead halide perovskites. *ACS Nano*, 11, 2017.

[22] G. Grancini et al. Role of microstructure in the electron-hole interaction of hybrid lead halide perovskites. *Nat. Photonics*, 9, 2015.

[23] L. Q. Phuong, Y. Yamada, M. Nagai, N. Maruyama, A. Wakamiya, and Y. Kanemitsu. Free carriers versus excitons in ch3nh3pbi3 perovskite thin films at low temperatures: Charge transfer from the orthorhombic phase to the tetragonal phase. *J. Phys. Chem. Lett.*, 7, 2016.

[24] C. S. Ponseca Jr. et al. Organometal halide perovskite solar cell materials rationalized: Ultrafast charge generation, high and microsecond-long balanced mobilities, and slow recombination. *J. Am. Chem. Soc.*, 14, 2014.

[25] S. D. Stranks, G. E. Eperon, G. Grancini, C. Menelaou, M. J. P. Alcocer, T. Leijtens, L. M. Herz, A. Petrozza, and H. J. Snaith. Electron-hole diffusion lengths exceeding 1 micrometer in an organometal trihalide perovskite. *Science*, 342, 2013.

[26] G. Xing, N. Mathews, S. Sun, S. S. Lim, Y. M. Lam, M. Gratzel, S. Mhaisalkar, and T. C. Sum. Long-range balanced electron- and hole-transport lengths in organic-inorganic ch3nh3pbi3. *Science*, 342, 2013.

[27] C. Wehrenfennig, M. Liu, H. J. Snaith, M. B. Johnston, and L. M. Herz. Charge-carrier dynamics in vapour-deposited films of the organolead perovskite ch3nh3pbi3-xclx. *Energy Environ. Sci.*, 7, 2014.

[28] D. Niesner, M. Wilhelm, I. Levchuk, A. Osvet, S. Shrestha, M. Batentschuk, C. Brabec, and T. Fauster. Giant rashba splitting in ch3nh3pbbr3 organic-inorganic perovskite. *Phys. Rev. Lett.*, 117, 2016.

[29] T. Wang, B. Daiber, J. M. Frost, S. A. Mann, E. C. Garnett, A. Walsh, and B. Ehrler. Indirect to direct bandgap transition in methylammonium lead halide perovskite. *Energy Environ. Sci.*, 10, 2017.

[30] K. Frohna et al. Inversion symmetry and bulk rashba effect in methylammonium lead iodide perovskite single crystals. *Nat. Comm.*, 9, 2018.

[31] H. Zhu, K. Miyata, Y. Fu, J. Wang, P. P. Joshi, D. Niesner, K. W. Williams, S. Jin, and X.-Y. Zhu. Screening in crystalline liquids protects energetic carriers in hybrid perovskites. *Science*, 353, 2016.

[32] K. Miyata, D. Meggiolara, M. T. Trinh, P. P. Joshi, E. Mosconi, S. C. Jones, F. De Angelis, and X. Y. Zhu. Large polarons in lead halide perovskites. *Sci. Adv.*, 3, 2017.

[33] D. Niesner, H. Zhu, K. Miyata, P. P. Joshi, T. J. S. Evans, B. J. Kudisch, M. T. Trinh, M. Marks, and X.-Y. Zhu. Persistent energetic electrons in methylammonium lead iodide perovskite thin films. *J. Am. Chem. Soc.*, 138, 2016.

[34] K. Miyata, T. L. Atallah, and X.-Y. Zhu. Lead halide perovskites: Crystal-liquid duality, phonon glass electron crystals, and large polaron formation. *Sci. Adv.*, 3, 2017.

[35] M. B. Price and Jet al. Hot-carrier cooling and photoinduced refractive index changes in organic-inorganic lead halide perovskites. *Nat. Comm.*, 6, 2015.

[36] J. Yang et al. Acoustic-optical phonon up-conversion and hot-phonon bottleneck in lead-halide perovskites. *Nat. Comm.*, 8, 2017.

[37] J. Fu, Q. Xu, G. Han, B. Wu, C. H. A. Huan, M. L. Leek, and T. C. Sum. Hot carrier cooling mechanisms in halide perovskite. *Nat. Comm.*, 8, 2017.

[38] Y. Yang, D. P. Ostrowski, R. M. France, K. Zhu, J. van de Lagemaat, J. M. Luther, and M. C. Beard. Observation of hot-phonon bottleneck in lead-iodide perovskites. *Nat. Photonics*, 10, 2015.

[39] M. Li, S. Bhaumik, T. W. Goh, M. S. Kumar, N. Yantara, M. Gratzel, S. Mhaisalkar, N. Mathews, and T. C. Sum. Slow cooling and highly efficient extraction of hot carriers in colloidal perovskite nanocrystals. *Nat. Comm.*, 8, 2017.

[40] A. D. Wright, C. Verdi, R. L. Milot, G. E. Eperon, M. A. Perez-Osorio, H. J. Snaith, F. Giustino, M. B. Johnston, and L. M. Herz. Electron-phonon coupling in hybrid lead halide perovskites. *Nat. Comm.*, 7, 2016.

[41] L. Luo et al. Ultrafast terahertz snapshots of excitonic rydberg states and electronic coherence in an organometal halide perovskite. *Nat. Comm.*, 8, 2017.

[42] C. La o-vorakiat et al. Phonon mode transformation across the orthorhombic-tetragonal phase transition in a lead iodide perovskite ch3nh3pbi3: A terahertz time-domain spectroscopy approach. *Phys. Chem. Lett.*, 7, 2015.

[43] C. La o-vorakiat et al. Elucidating the role of disorder and free-carrier recombination kinetics in ch3nh3pbi3 perovskite films. *Nat. Comm.*, 6, 2015.

[44] A. J. Frenzel. *Teraherz Electrodynamics of Dirac Fermions in Two-Dimensional Materials*. PhD thesis, Cambridge, Massachusetts, 2015.

[45] S. L. Dexheimer. *Terahertz Spectroscopy: Principles and Applications*. CRC Press, Boca Raton, FL, 2008.

[46] D. von Andreas Paulke. *Transient Conductivity Measurements using Terahertz Time-Domain Spectroscopy*. PhD thesis, 2013.

[47] P. C. M. Planken, H.-K. Nienhuys, H. J. Bakker, and T. Wenckebach. Measurement and calculation of the orientation dependence of terahertz pulse detection in znte. *J. Opt. Soc. Am. B*, 18, 2001.

[48] L. Duvillaret, F. Garet, and J.-L. Coutaz. A reliable method for extraction of material parameters in terahertz time-domain spectroscopy. *IEEE J. Sel. Top. Quant.*, 2, 1996.

[49] L. Duvillaret, F. Garet, and J.-L. Coutaz. Highly precise determination of optical constants and sample thickness in terahertz time-domain spectroscopy. *App. Optics*, 38, 1999.

[50] H.-K. Nienhuys and V. Sundstrom. Intrinsic complications in the analysis of optical-pump, terahertz probe experiments. *Phys. Rev. B*, 71, 2005.

[51] N. V. Smith. Classical generalization of the drude formula for the optical conductivity. 64, 2001.

[52] J. B. Baxter and C. A. Schmuttenmaer. Conductivity of zno nanowires, nanoparticles, and thin films using time-resolved terahertz spectroscopy. *J. Phys. Chem. B*, 110, 2006.

[53] I. Pupeza, R. Wilk, , and M. Koch. Highly accurate optical material parameter determination with thz time-domain spectroscopy. *Optics Express*, 15, 2007.

[54] G. Xing, N. Mathews, S. S. Lim, N. Yantara, X. Liu, D. Sabba, M. Gratzel, S. Mhaisalkar, and T. C. Sum. Low-temperature solution-processed wavelength-tunable perovskites for lasing. *Nat. Mater.*, 13, 2014.

[55] S. Adjokatse, H.-H. Fang, and M. A. Loi. Broadly tunable metal halide perovskites for solid-state light-emission applications. *Mater. Today*, 20, 2017.

[56] Z. Yang et al. Unraveling the exciton binding energy and the dielectric constant in single crystal methylammonium lead tri-iodide perovskite. *J. Phys. Chem. Lett.*, 8, 2017.

[57] K. P. O'Donnell and X. Chen. Temperature dependence of semiconductor band gaps. *Appl. Phys. Lett.*, 58, 1991.

[58] F. Panzer et al. Reversible laser-induced amplified spontaneous emission from coexisting tetragonal and orthorhombic phases in hybrid lead halide perovskites. *Adv. Opt. Mater.*, 4, 2016.

[59] X. Chen, H. Lu, Y. Yang, and M. C. Beard. Excitonic effects in methylammonium lead halide perovskites. *J. Phys. Chem. Lett.*, 9, 2018.

[60] D.-J. Heijs, A. G. Dijkstra, and J. Knoester. Ultrafast pump-probe spectroscopy of linear molecular aggregates. *Chem. Phys.*, 341, 2007.

[61] H. Wang, L. Whittaker-Brooks, and G. R. Fleming. Exciton and free charge dynamics of methylammonium lead iodide perovskites are different in the tetragonal and orthorhombic phases. *J. Phys. Chem. C*, 119, 2015.

[62] Y. Wang, X. Li, X. Zhao, L. Xiao, H. Zeng, and H. Sun. Nonlinear absorption and low-threshold multiphoton pumped stimulated emission from all-inorganic perovskite nanocrystals. *Nano Lett.*, 16, 2016.

[63] H. Yan, B. An, Z. Fan, Z. Zhu, X. Lin, Z. Jin, and G. Ma. Ultrafast terahertz probe of photoexcited free charge carriers in organometal ch3nh3pbi3 perovskite thin film. *Appl. Phys. A*, 122, 2016.

[64] J. M. Frost and Aron Walsh. What is moving in hybrid halide perovskite solar cells? *Acc. Chem. Res.*, 49, 2016.

[65] D. Li, G. Wang, H.-C. Cheng, C.-Y. Chen, H. Wu, Y. Liu, Y. Huang, and X. Duan. Size-dependent phase transition in methylammonium lead iodide perovskite microplate crystals. *Nat. Comm.*, 7, 2016.

[66] I. Levine et al. *J. Phys. Chem. C*, 120, 2016.

[67] H. Huang, L. Polavarapu, J. A. Sichert, A. S. Susha, and A. S. Urban. Colloidal lead halide perovskite nanocrystals: synthesis, optical properties and applications. *NPG Asia Materials*, 6, 2016.

[68] P. Perumal, C.-S. Wang, K. M. Boopathi, G. Haider, W.-C. Liao, and Y.-F. Chen. Whispering gallery mode lasing from self-assembled hexagonal perovskite single crystals and porous thin films decorated by dielectric spherical resonators. 4, 2017.

[69] H. Zhu, Y. Fu, F. Meng, X. Wu, Z. Gong, Q. Ding, M. V. Gustafsson, M. T. Trinh, S. Jin, and X. Y. Zhu. Lead halide perovskite nanowire lasers with low lasing thresholds and high quality factors. *Nat. Mater.*, 6, 2015.

APPENDICES

Appendix A

Supplementary Information

A.1 Excitation density

Excitation density is calculated as

$$n_{ex} = (1 - e^{-\alpha(\omega)l})\alpha(\omega)E_{pulse}/\hbar\omega A_{pulse}, \tag{A.1}$$

where $\alpha(\omega) = ln(10) \cdot OD$ is the absorption at the pump frequency according to the absorption spectrum in (fig.4.1a), l is the sample thickness, E_{pulse} is the energy per pump pulse, and A_{pulse} is the pump area on the sample. Note that we have approximated the carrier distribution as a rectangular slab with depth of $1/\alpha$, whereas the true carrier distribution decays exponentially away from the surface with a decay constant of α.

A.2 Effects of repeated cooling cycling on TP inclusions

We found that ASE occurs only once TP inclusions are filled, and so smaller inclusions (for example, at lower temperature) should be found to have a lower ASE threshold. Previous studies have found that repeated temperature cycling and the repeated formation of TP inclusions results in permanent damage to the crystal structure upon reheating [65]. To explore this effect, we performed three cycles of reheating to 295K, cooling to 80K, and measuring PL. On the 1st cycle, we observed ASE from both TP and OP, but on the 2nd cycle OP PL had decreased and ASE was only observed from TP, suggesting that carrier transfer to TP was more efficient. Each cycle of cooling and reheating creates crystal defects which increase the number of TP inclusions at low temperature, thus suppressing ASE from OP. On the 3rd cycle, we reheated

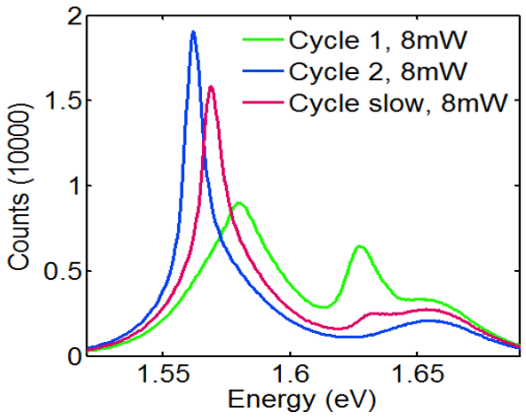

Figure A.1

the sample at 10% heater power, and upon cooling found that OP ASE had somewhat returned, implying that the disorder created by previous cycles had been partially healed.

A.3 Density independence of upper band tails

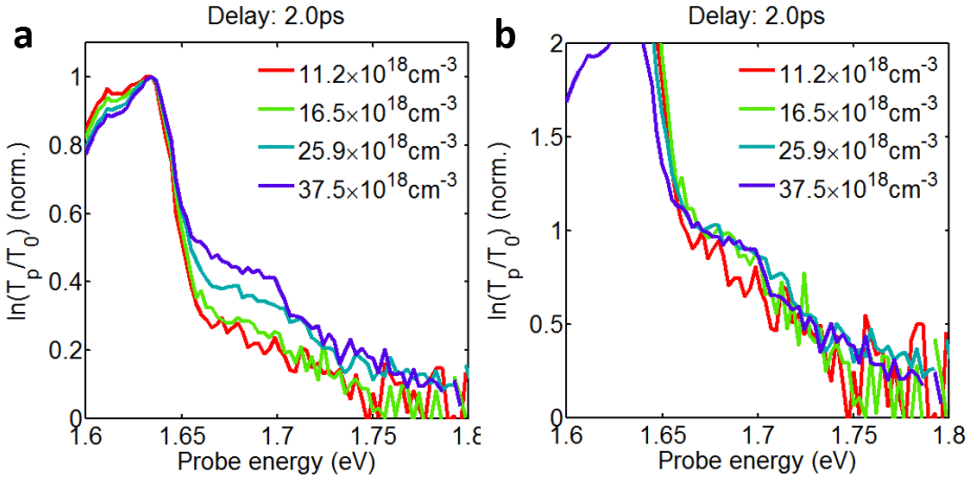

Figure A.2

(a) Normalized at 1.63eV to confirm that high-energy tail of PB_T is not broadened with increasing excitation density, though this region is obscured by SE_O and PB_O. (b) Normalized

at 1.67eV to confirm that high-energy of tail of PB_O is not broadened with increasing excitation density.

Appendix B

Simulated example of transient absorption analysis

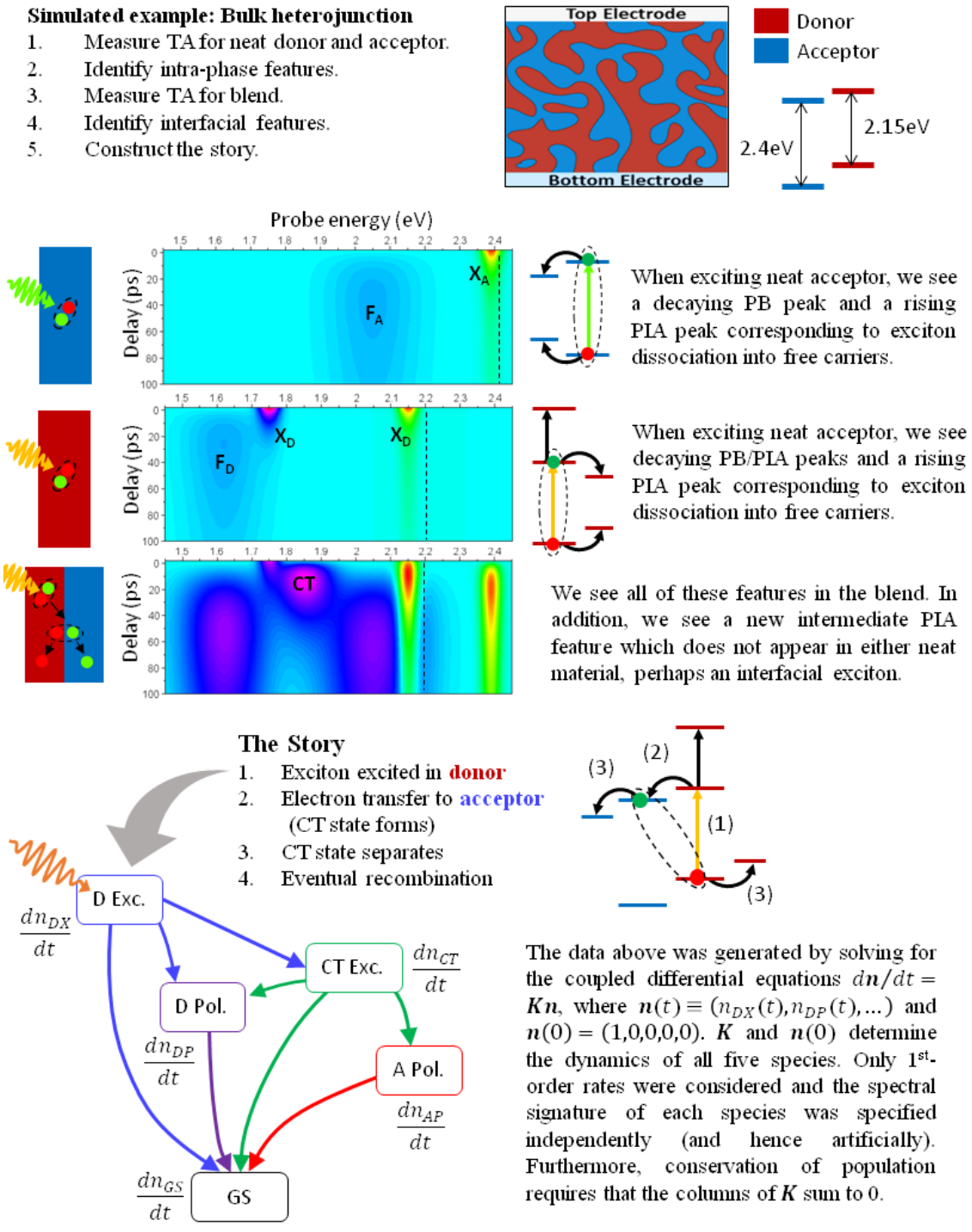
Simulated example: Bulk heterojunction
1. Measure TA for neat donor and acceptor.
2. Identify intra-phase features.
3. Measure TA for blend.
4. Identify interfacial features.
5. Construct the story.
Top Electrode
Bottom Electrode
Donor
Acceptor
2.4eV
2.15eV
Probe energy (eV)
Delay (ps)
X_A
F_A
X_D
F_D
CT
When exciting neat acceptor, we see a decaying PB peak and a rising PIA peak corresponding to exciton dissociation into free carriers.
When exciting neat acceptor, we see decaying PB/PIA peaks and a rising PIA peak corresponding to exciton dissociation into free carriers.
We see all of these features in the blend. In addition, we see a new intermediate PIA feature which does not appear in either neat material, perhaps an interfacial exciton.
The Story
1. Exciton excited in donor
2. Electron transfer to acceptor (CT state forms)
3. CT state separates
4. Eventual recombination
(1)
(2)
(3)
(3)
D Exc.
CT Exc.
D Pol.
A Pol.
GS
$\frac{dn_{DX}}{dt}$
$\frac{dn_{CT}}{dt}$
$\frac{dn_{DP}}{dt}$
$\frac{dn_{AP}}{dt}$
$\frac{dn_{GS}}{dt}$
The data above was generated by solving for the coupled differential equations $d\boldsymbol{n}/dt = \boldsymbol{K}\boldsymbol{n}$, where $\boldsymbol{n}(t) \equiv (n_{DX}(t), n_{DP}(t), \ldots)$ and $\boldsymbol{n}(0) = (1,0,0,0,0)$. $\boldsymbol{K}$ and $\boldsymbol{n}(0)$ determine the dynamics of all five species. Only 1st-order rates were considered and the spectral signature of each species was specified independently (and hence artificially). Furthermore, conservation of population requires that the columns of $\boldsymbol{K}$ sum to 0.

Figure B.1